ELSEVIER

Comput. Methods Appl. Mech. Engrg. 190 (2001) 6089–6124

Computer methods in applied mechanics and engineering

www.elsevier.com/locate/cma

Estimation of local modeling error and goal-oriented adaptive modeling of heterogeneous materials Part II: a computational environment for adaptive modeling of heterogeneous elastic solids

Kumar S. Vemaganti *, J. Tinsley Oden

Texas Institute for Computational and Applied Mathematics (TICAM), The University of Texas at Austin, 201 E 24th Street, ACES 6.412, Austin, TX 78712, USA

Received 13 October 2000; received in revised form 18 December 2000

Abstract

This paper addresses a classical and largely unsolved problem: given a structural component constructed of a heterogeneous elastic material that is in equilibrium under the action of applied loads, determine local micromechanical features of its response (e.g., local stresses and displacements in or around phase boundaries or in inclusions) to an arbitrary preset level of accuracy, it being understood that the microstructure is a priori unknown, may be randomly distributed, may exist at multiple spatial scales, and may contain millions, even billions, of microscale components. The approach described in this work begins with a mathematical abstraction of this problem in which the material body is modeled as an elastic solid with highly variable, possibly randomly distributed, elastic properties. Information on the actual character of the microstructure of given material bodies is determined by computerized tomography (CT) imaging. A procedure is given for determining the effective material properties from imaging data, using either deterministic or stochastic methods. An algorithm is then described for determining local quantities of interest, such as average stresses on inclusion boundaries, to arbitrary accuracy relative to the fine-scale model. A new computational environment for implementing such analyses is presented which employs parallel, adaptive, hp finite element methods, CT interfaces, automatic meshing procedures, and, effectively, adaptive modeling schemes. Within the basic premises on which the approach is based, results of any specified accuracy can be obtained, independently of the number of microscale components and constituents. The results of several numerical experiments are presented.

Keywords: Heterogeneous materials; Modeling error; Local error estimates

1. Introduction

It is well known that the service life and performance of structural components, machine parts, and general material bodies often depend upon micromechanical events that take place at scales much smaller then those prevalent in traditional macromechanical characterizations of material properties. On the other hand, in the actual analysis of real components, the geometry, properties, and distribution of the microstructure is rarely known and is impossible to determine without the use of special technologies. Moreover, in most engineering materials, the number of microstructural components is enormous, often exceeding millions of constituents, and the geometry, orientation, and mechanical properties are unknown or not known with significant precision. Thus, a detailed analysis of micromechanics is regarded as impossible,

* Corresponding author. Tel.: +1-512-471-3312; fax: +1-512-471-8694.
E-mail address: kumar@ticam.utexas.edu (K.S. Vemaganti).

0045-7825/01/$ - see front matter
PII: S0045-7825(01)00217-1

well beyond the scope of any conceivable computational strategy. It is this somewhat paradoxical situation that has led to the study of methods to extract "effective properties" of materials, a subject that has dominated research on the mechanics of materials for a half-century or more.

In this investigation, we present a general approach, and a computational strategy, for determining local micromechanical features of the response of arbitrary, heterogeneous, elastic bodies in equilibrium under the action of prescribed external forces. The approach can be applied independently of the number of microscale constituents and can, in a sense to be made precise below, yield computed values of quantities of interest with an accuracy predefined by the user.

Naturally, the approach is based on a number of critical assumptions. Firstly, the actual, physical structure is replaced by a mathematical model which depicts the body as a heterogeneous elastic body with rapidly varying coefficients. These coefficients and their variation over the body (or, equivalently, the number of constituents and their mechanical properties) are, a priori, unknown. Secondly, we assume that the microstructure can be characterized with adequate precision by the use of imaging technologies: in our case, computerized tomography (CT) images generated by X-ray devices. We may then identify "quantities of interest" which are specific local features of the response that are identified a priori as important in design considerations, or in determining the local conditions within the material. Such local quantities of interest could represent, for example, average normal or shear stresses on material interfaces, displacements of inclusions, relative displacements of particles in a material matrix, etc. Mathematically, such quantities of interest are characterized as continuous linear functionals on the class of admissible functions to which the fine-scale solution of the problem belongs. In a previous paper [24], computable a posteriori bounds on the error (and estimates of the error) in the quantities of interest due to evaluating them using a "homogenized solution" of the problem were derived. These estimates provide a basis for adaptive modeling of the quantities of interest. This is accomplished by using an algorithm, referred to as the goal oriented adaptive local solution (GOALS) algorithm in our companion paper [24], which utilizes CT data and automatic meshing schemes to augment the analysis procedures.

It is clear that the assumptions underlying our approach may be invalid in many cases or they may be insufficient in themselves to allow a complete resolution of the target problem. These assumptions can be weakened and the approach generalized. It is well known that local damage or plastic deformation can occur in heterogeneous materials, even under moderate loads. To account for such effects, the model problem class that serves as a datum against which modeling errors are measured must be extended to include nonlinear effects. Such extensions of the approach can be accomplished by expanding the equations governing the model to include specific nonlinear effects and using the GOALS algorithm each step of the iterative procedure. Discussions of such extensions are given in preliminary reports [21,22].

In addition, CT imaging is subject to well-known imprecisions. Firstly, available CT devices are capable of resolutions of around 10 μm; features at smaller scales are thus lost. To resolve finer-scale attributes, other imaging modalities must be employed, but most require an invasion of the microstructure by various means which for many applications may be unacceptable. Secondly, the CT image itself is imperfect, as it depends on the threshold levels selected for gray-scale shadings assigned to pixel arrays defining the image. This is the problem of *segmentation*, and is critical in determining an accurate representation of internal features in a nondestructive process. We discuss one approach for addressing this problem in Section 3 of this work. Thirdly, CT imaging yields only density maps of slices of the specimen, and does not provide information on the mechanical properties of the microscale constituents. Such microproperties must generally be inferred from additional information gathered on the material. This information can possibly be obtained from micromechanical tests (e.g., nanoindentation tests, which may also be subject to significant errors), from other models of sub-scale physics (e.g., molecular dynamics models), or can be determined from independent tests on constituents prior to the fabrication of the specimen (such as in the manufacturing of multi-phase composites). In the present work, we confine our attention to n-phase composites (n generally two or three) in which the mechanical properties are known a priori and for which the geometry of individual components is rather simple; typically spherical or cylindrical. Our approach, however, is applicable to materials with quite general microstructural features provided they are resolvable by the CT device in hand.

We review briefly the major features of the GOALS algorithm in Section 2. We then present the details of a general computational system designed to deliver high-fidelity predictions of local response features of

structural components which fall into the class covered adequately by our initial assumptions. For problems in this class, the approach, as indicated earlier, yields results of arbitrary, preset accuracy, is independent of the number and distribution of microstructural constituents, makes use of imaging data to represent micromechanical properties to the extent required in the adaptive modeling algorithm (GOALS), provides automatic meshing of sample representative volume elements (RVEs) using imaging data, and involves highly accurate numerical approximations of various boundary value problems (BVPs) generated in the process obtained using a parallel, adaptive, hp finite element solver and a systematic partitioning and load balancing technique based on the notion of space filling curves (SFCs) [26]. Details of all these aspects of our approach are covered in the remainder of this paper.

Following a review of the basic strategies, we describe the integration of CT imaging and parallel hp adaptive finite element analyses to determine effective properties of various specimens, a key step in the basic approach. The architecture of the software developed to implement the strategy is briefly summarized. Finally, we present the results of several experiments which test the validity of the approach and which demonstrate its performance on a suite of model problems. Included in these tests are cases in which physical specimens have been fabricated which are two-phase composites comprised of an epoxy matrix and spherical glass inclusions. The final section contains concluding remarks.

2. Preliminaries: the adaptive modeling strategy

Our purpose here is to provide an overview of the general computational environment that is the objective of this work, and to then provide further detail on the individual components in subsequent sections.

The general ideas of the adaptive-modeling algorithm depicted in Fig. 1, are:

1. a structural component is given or fabricated and a list of analysis goals, so-called *quantities of interest*, is identified; the accurate calculation of these quantities is the goal of the analysis;
2. X-ray tomography is used to scan the specimen or various portions of it to approximately define the internal microstructure;
3. a homogenization module accepts imaging data taken from sampled sections of the body and computes effective mechanical properties using an adaptive finite element method;

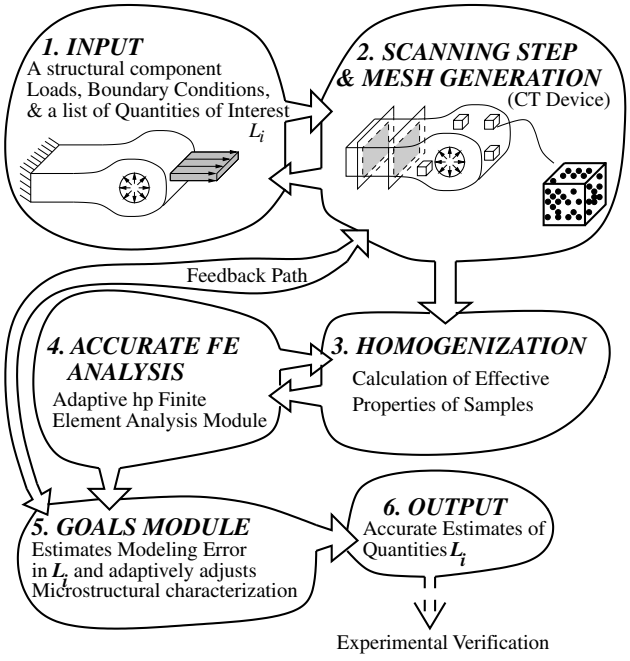

Fig. 1. Schematic of the adaptive modeling strategy.

4. the effective properties are used as input data in the adaptive hp finite element program which computes a highly accurate "homogenized" solution to the equations of elastostatics for given loading and applied force data (a step in which the response of the body is modeled mathematically as a homogeneous, linearly elastic body);
5. the homogenized solution is input to a module which implements the GOALS algorithm which estimates the errors in the quantities of interest (errors due to modeling the heterogeneous material as a homogenized medium) and adaptively adjusts the calculated quantities (by using additional microscale data supplied by the imaging process) until preset levels of accuracy are attained;
6. the output is the set of quantities of interest; when possible, these results are verified by independent physical experiments.

In general, there is feedback between steps 1 and 2, and steps 5 and 2: from 2 to 1, as imaging data may be needed to identify quantities of interest, and from 5 to 2, as additional imaging data on microstructure may be needed to adaptively improve the accuracy of the model. Further discussion of these steps is given below.

2.1. Goals of the analysis: quantities of interest

The target problem is this: given a structural component subjected to known boundary conditions and loads, determine its response to these external loads. In the present investigation, it is assumed that

1. the body is linearly elastic;
2. the exterior geometry, boundary conditions, and applied external forces are known exactly; [1]

By "response", we generally mean the displacement and stress fields within the body or some well-defined functions of these fields.

In virtually all applications having to do with engineering analysis and design or with determining the performance of the component to design loads, the analyst is interested in a finite (generally small) list of special local features of the response, such as local stresses on internal inclusions in the body, average stresses on material interfaces, relative displacements of constituents, average displacement, shear stress, or normal stress on internal surfaces, etc. Our goal shall be the accurate determination of such local quantities of interest. If each such quantity be labeled L_i, $1 \leqslant i \leqslant N_L$, then our goal is to determine, with a prescribed and quantifiable level of accuracy, the set $\mathscr{L} = \{L_i\}_{i=1}^{N_L}$.

2.2. Imaging

It is further assumed that

1. while the internal microstructure of the body is unknown, it can be determined with sufficient accuracy by the use of imaging devices such as X-ray tomography.

The microstructure is characterized by the geometric shape, orientation, distribution, and mechanical properties of various constituents and by the volume fraction of certain "phases" of material. While our approach is applicable to bodies with many such phases, each phase is assumed to be linearly elastic and to have mechanical properties (elasticities) that are a priori known. In some cases, including cases described later, the actual fabrication of the component is done as a precursor to the implementation of the analysis process. Then, mechanical properties of some of the microstructural features may be known with high precision.

The imaging field of typical CT imaging devices is often much smaller than the physical dimensions of the specimen (the structural component). Thus, CT imaging may be used to depict microstructural features

[1] Of course, a natural question, in practical applications, is how does one determine the actual loads and boundary conditions on various structural components? In general, such loads and conditions are obtained, albeit approximately, from a global analysis of a larger assemblage, of which the component of interest is a unit. Forces and restraints on the assemblage are also presumed to be known, perhaps with better precision than those on components. The response of the component can, therefore, change the nature of the loads acting on it. Then the process described here is only one step in an iterative global–local procedure in which final loads are determined by a sequence of corrections of an initial analysis.

(topology and geometric features) of *samples* of the material. We will use such sample images to determine effective properties of the heterogeneous material. As will be seen later, such approximate effective properties may be highly inaccurate; nevertheless, a method for calculating effective properties from sample CT images is an important part of the computational procedure.

2.3. The mathematical model

Now the actual response of the material body under study can be thought of as being depicted by a mathematical abstraction, a mathematical model, provided (in this investigation) by the equations of linear elasticity for heterogeneous bodies:

$$\begin{aligned} &-\operatorname{div}\mathbf{E}(\mathbf{x})\nabla\mathbf{u}(\mathbf{x}) = \mathbf{f}(\mathbf{x}), \quad \mathbf{x}\in\Omega,\\ &\mathbf{n}(\mathbf{x})\cdot\mathbf{E}(\mathbf{x})\nabla\mathbf{u}(\mathbf{x}) = \mathbf{t}(\mathbf{x}), \quad \mathbf{x}\in\Gamma_t,\\ &\mathbf{u}(\mathbf{x}) = \mathscr{U}(\mathbf{x}), \quad \mathbf{x}\in\Gamma_u. \end{aligned} \tag{1}$$

Here, $\Omega\subset\mathbb{R}^N$ $(N=1,2,3)$ is the open interior of the material body under consideration, Γ_t and Γ_u are portions of the boundary $\partial\Omega$ of Ω on which tractions $\mathbf{t}$ and displacements $\mathscr{U}$, respectively, are prescribed, $\mathbf{f}$ is the body force per unit volume, and $\mathbf{n}$ is the unit exterior normal to $\partial\Omega$. In (1):

$\mathbf{E}(\mathbf{x}) =$ the value of the elasticity tensor $\mathbf{E}$ at a point $\mathbf{x}\in\Omega$;

$\mathbf{u}(\mathbf{x}) =$ the value of the fine-scale displacement field $\mathbf{u}$ at a point $\mathbf{x}\in\Omega$.

It will always be assumed that $\mathbf{E}$ has the standard symmetries and ellipticity properties of elasticity tensors: $E_{ijkl}(\mathbf{x}) = E_{jikl}(\mathbf{x}) = E_{ijlk}(\mathbf{x}) = E_{klij}(\mathbf{x})$, for a.e $\mathbf{x}\in\Omega, 1\leqslant i,j,k,l\leqslant N$; there exist constants $\alpha_0,\alpha_1>0$ such that for almost all $\mathbf{x}\in\Omega$,

$$\alpha_0\varepsilon_{ij}\varepsilon_{ij}\leqslant E_{ijkl}(\mathbf{x})\varepsilon_{ij}\varepsilon_{kl}\leqslant\alpha_1\varepsilon_{ij}\varepsilon_{ij} \tag{2}$$

for any $\varepsilon_{ij}\in\mathbb{R}^N\times\mathbb{R}^N, \varepsilon_{ij}=\varepsilon_{ji}$, and repeated indices are summed throughout their range, $1\leqslant i,j,k,l\leqslant N$. Owing to the possibly very irregular distribution of multi-phase microstructural features within the body, $\mathbf{E}$ will, in general, be a highly oscillatory, rapidly varying function of $\mathbf{x}$.

It is emphasized that the function $\mathbf{E}=\mathbf{E}(\mathbf{x})$ *will rarely ever be completely known, and therefore, the fine-scale displacement field* $\mathbf{u}=\mathbf{u}(\mathbf{x})$ *will also never (or rarely ever) be known*. The best that one can usually hope for is that a CT imaging device can be used to *sample* the specimen and determine an approximate restriction of $\mathbf{E}$ to the sampled subdomains.

2.4. Effective properties: the homogenized problem

Since our knowledge of $\mathbf{E}$ is incomplete and since the fine-scale displacement field is unknown and generally impossible to determine, we resort to an old and classical approach used to analyze heterogeneous media: the elasticity tensor $\mathbf{E}$ is replaced by a smeared, or homogenized tensor $\mathbf{E}^0$ of *effective properties*.

In our adaptive modeling process, imaging data from the samples is used to compute such effective properties. This is accomplished by generating a finite element mesh of the microstructure and calling an hp finite element module (discussed below) to calculate effective moduli. It is emphasized that the determination of effective properties is not the goal of this analysis; homogenization is only an artifact in a broader computational strategy. Thus, in the present approach,

- $\mathbf{E}^0$ is computed from data supplied by the CT image of samples of the body;
- $\mathbf{E}^0$ may be a constant tensor, or it can vary over a large group of samples, being constant, however, over each sample.

$\mathbf{E}^0$ can be computed from sample data on the microstructure using the well-known theories of homogenization [5,28], or it can be approximated using well-accepted bounds on effective properties of heterogeneous materials [12]. With $\mathbf{E}^0$ known, we replace (1) by the *homogenized problem*:

$$
\begin{aligned}
&-\operatorname{div}\mathbf{E}^0\nabla\mathbf{u}^0(\mathbf{x}) = \mathbf{f}(\mathbf{x}), \quad \mathbf{x}\in\Omega,\\
&\mathbf{n}(\mathbf{x})\cdot\mathbf{E}^0(\mathbf{x})\nabla\mathbf{u}^0(\mathbf{x}) = \mathbf{t}(\mathbf{x}), \quad \mathbf{x}\in\Gamma_t,\\
&\mathbf{u}^0(\mathbf{x}) = \mathscr{U}(\mathbf{x}), \quad \mathbf{x}\in\Gamma_u.
\end{aligned}
\tag{3}
$$

The displacement field $\mathbf{u}^0 = \mathbf{u}^0(\mathbf{x})$ is called the *homogenized displacement field*. While we do not know the fine-scale field $\mathbf{u}$, we can nevertheless estimate quite accurately, the *homogenization error*

$$
\mathbf{e}^0 = \mathbf{u} - \mathbf{u}^0 \tag{4}
$$

using methods described in [24,31].

2.5. Weak forms, error norms, and finite element analysis

It is well known that for general domains Ω and general loading and boundary conditions, classical solutions to problems (1) and (3) do not exist. One is then led to consider weak or variational forms. In the case of (1), we have the corresponding weak problem:

$$
\text{Find } \mathbf{u}\in\{\hat{\mathbf{u}}\}+\mathbf{V}(\Omega) \text{ such that } \mathscr{B}_\Omega(\mathbf{u},\mathbf{v}) = \mathscr{F}_\Omega(\mathbf{v})\ \forall\mathbf{v}\in\mathbf{V}(\Omega). \tag{5}
$$

Here, $\mathbf{V}(\Omega)$ is the space of admissible displacements

$$
\mathbf{V}(\Omega)\stackrel{\text{def}}{=}\left\{\mathbf{v}\in\left(H^1(\Omega)\right)^N : \mathbf{v}=\mathbf{0} \text{ on } \Gamma_u\right\}. \tag{6}
$$

Also, $\hat{\mathbf{u}}$ is an $(H^1(\Omega))^N$ function whose trace on Γ_u is the Dirichlet data $\mathscr{U}$, and

$$
\mathscr{B}_\Omega(\mathbf{u},\mathbf{v})\stackrel{\text{def}}{=}\int_\Omega \nabla\mathbf{v} : \mathbf{E}\nabla\mathbf{u}\,\mathrm{d}\mathbf{x}, \tag{7}
$$

$$
\mathscr{F}_\Omega(\mathbf{v})\stackrel{\text{def}}{=}\int_\Omega \mathbf{f}\cdot\mathbf{v}\,\mathrm{d}\mathbf{x}+\int_{\Gamma_t}\mathbf{t}\cdot\mathbf{v}\,\mathrm{d}\mathbf{s}. \tag{8}
$$

In (7), the integrand is an $L^1(\Omega)$ function,

$$
\nabla\mathbf{v} : \mathbf{E}\nabla\mathbf{u} = \frac{\partial v_i}{\partial x_j}(\mathbf{x})E_{ijkl}(\mathbf{x})\frac{\partial u_k}{\partial x_l}(\mathbf{x})
$$

(repeated indices summed; $1\leqslant i,j,k,l\leqslant N, N=1,2,3$). In (8), it is implicitly assumed that $\mathbf{f}\in(L^2(\Omega))^N$ and $\mathbf{t}\cdot\mathbf{v}$ is integrable on Γ_t for $\mathbf{v}\in\mathbf{V}(\Omega)$.

The weak form of the homogenized problem (3) is:

$$
\text{Find } \mathbf{u}^0\in\{\hat{\mathbf{u}}\}+\mathbf{V}(\Omega) \text{ such that } \mathscr{B}^0_\Omega(\mathbf{u}^0,\mathbf{v}) = \mathscr{F}_\Omega(\mathbf{v})\ \forall\mathbf{v}\in\mathbf{V}(\Omega), \tag{9}
$$

where

$$
\mathscr{B}^0_\Omega(\mathbf{u}^0,\mathbf{v})\stackrel{\text{def}}{=}\int_\Omega \nabla\mathbf{v} : \mathbf{E}^0\nabla\mathbf{u}^0\,\mathrm{d}\mathbf{x}, \tag{10}
$$

and $\mathbf{E}^0$ denotes the elasticity tensor for the homogenized problem.

The analysis of these problems and the periodic BVPs used in determining the effective properties (in step 3 in Fig. 1) is done using a parallel, hp adaptive finite element method designed to deliver highly accurate solutions for $\mathbf{u}^0$ (and $\mathbf{E}^0$) with estimatable approximation error. The GOALS algorithm in step 5 also employs this tool to compute the solutions of local BVPs of the type

$$
\mathscr{B}_\omega(\tilde{\mathbf{u}},\mathbf{v}) = \mathscr{F}_\omega(\mathbf{v}) \quad \forall\mathbf{v}\in\mathbf{V}_\omega, \tag{11}
$$

where ω is a subdomain surrounding a local quantity of interest, in a sense made precise later. Here, $\tilde{\mathbf{u}}$ is a correction to $\mathbf{u}^0$ satisfying Dirichlet boundary conditions ($\tilde{\mathbf{u}}=\mathbf{u}^0$ on $\partial\omega\setminus\Gamma_t$, $\mathbf{n}\cdot\mathbf{E}\nabla\tilde{\mathbf{u}}=\mathbf{t}$ on $\partial\omega\cap\Gamma_t$).

As will be explained in more detail later, the quantities of interest $L_i \in \mathscr{L}$ are mathematically characterized as continuous linear functionals on $\mathbf{V}$:

$$L_i \in \mathbf{V}'(\Omega), \tag{12}$$

$\mathbf{V}'(\Omega)$ being the dual space of $\mathbf{V}(\Omega)$. The GOALS algorithm controls the modeling error in each L_i and estimates the value of the quantity itself.

When feasible, the predicted response produced by the adaptive modeling system should be compared with results of physical experiments. Such experimental verifications, of course, are difficult to obtain. We also comment on this topic further later in this work.

3. Computerized tomography and mesh generation

With the advent of high-precision imaging devices, the use of imaging techniques to obtain information about the microstructure of composites is becoming more prevalent. Such techniques are nondestructive in nature, i.e., they do not affect the service life or usability of a specimen. Typical imaging devices are scanning electron microscopes, optical microscopes and CT machines.

There is a growing volume of literature on the use of imaging technologies to characterize microscale properties of heterogeneous materials. As representative of this literature, we mention the work of London et al. [18] who use CT to observe microstructural damage caused by heating and thermal cycling in metal/matrix and carbon/carbon composites. Terada et al. [29] use a scanning electron microscope to obtain images of metal–matrix composites. This information is then used to compute effective properties of the specimens by treating each voxel from the image as a finite element. Michel et al. [19,20] propose a Fourier transform-based technique that directly uses imaging data to compute the effective properties of both linear and nonlinear composite materials.

Ghosh and Moorthy [9] have used micrographs of Al–Si–Mg composites to construct Voronoi cell finite element method (VCFEM)-based computational models for damage analysis. Using imaging data, Babuška et al. [2] studied the properties of fibrous composites, with an emphasis on the stochastic nature of the constitutive properties of the composite and the statistics of interfacial stresses. Huet [15] studied crack propagation in composites using a system that integrated imaging, mesh generation and finite element analysis. Additional references to work on the use of imaging techniques to obtain effective properties can be found in the papers cited here.

An important difference between previous works in this area and the current approach is that our goal is not to compute effective properties of samples by imaging them. Neither is our goal to extract complete microstructural information about a specimen in order to compute a fine-scale solution. Indeed, our approach consists of combining imaging techniques with adaptive material modeling procedures in order to compute quantities of interest with high accuracy.

3.1. CT imaging

Tomography refers to the cross-sectional imaging of an object from data collected by subjecting the object to electro-magnetic radiation from different directions. X-ray CT refers to the use of X-rays to analyze a given cross-section. Since a 3-D description of an object can, in principle, be assembled from a series of 2-D (planar) descriptions, we focus our attention here on the analysis of 2-D CT images.

The output from the CT analysis of a material is a planar map of the attenuation coefficient [2] of the material, given as a discrete function over a cartesian grid in the form of a gray-scale. Each element of this grid is termed a *pixel*.

[2] The attenuation coefficient of a material, as the name suggests, measures the attenuation or the loss of intensity of an X-ray while passing through the material as a result of the Photoelectric absorption effect and the Compton effect. In general, the attenuation coefficient of a material can be related accurately to material densities.

For a detailed discussion of CT imaging, see [17]. In the current study, we use a X-ray CT device with a resolution of about 10 μm.

3.2. The segmentation problem

Segmentation refers to the process of identifying individual constituents and the interfaces between constituents in a material from its gray-scale image. For a two-phase material, this amounts to classifying a pixel as belonging to one of two materials and grouping like pixels. The range of the gray-scale depends on the number of "bits" of information stored per pixel; an 8-bit gray-scale, for instance, ranges from 0 to 255 in value. Thus, to segment an image of a two-phase material, it is necessary to select a threshold value, above which a pixel is considered to be of one material, and below which the pixel belongs to the other material. For multi-phase materials, several threshold values must be identified to delineate various micromechanical constituents. The choice of this threshold value, evidently, has a significant impact on the outcome of the segmentation process. Once the threshold parameter, also known as an isovalue, is selected, the isocontour – the surface on which the value of the gray-scale function equals the selected isovalue – has to be determined. Here, we comment only about the selection of the isovalue; a discussion of isocontouring is beyond the scope of this paper.

Our approach to the segmentation problem consists of augmenting the Contour Spectrum approach proposed by Bajaj et al. [4] with known information about the specimen. In particular, we use information about the volume fraction of the specimen to arrive at a segmented image. In the current approach, the threshold value is varied from one end of the gray-scale to the other, and for each value of the threshold parameter, the volume fraction of the resulting segmented image is computed. Then, the threshold value that predicts the known volume fraction of the specimen is selected as the true threshold value. For more details on the Contour Spectrum approach and the isocontouring algorithms used in this work, see [3,4].

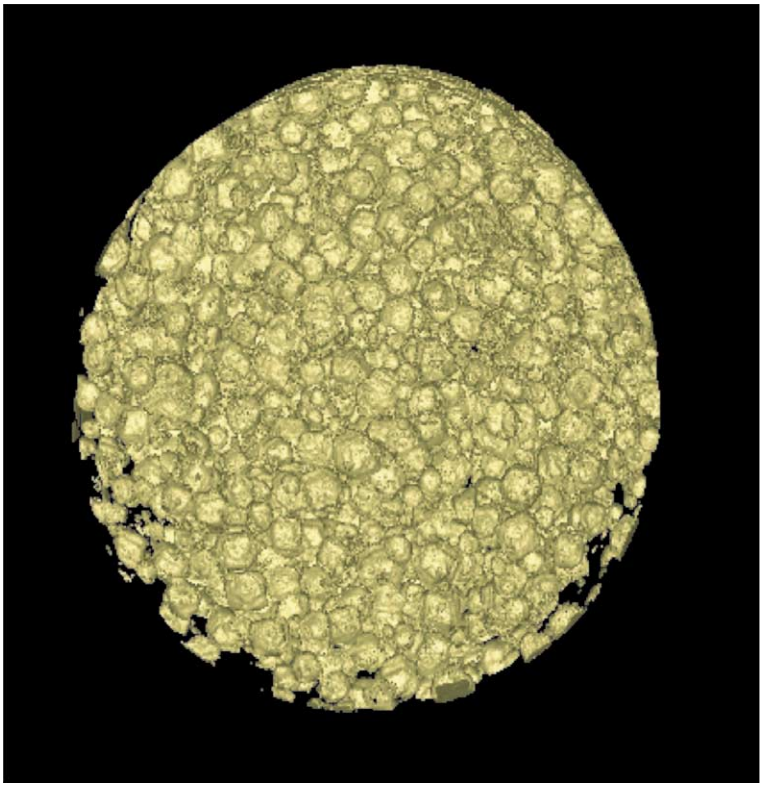

Fig. 2. CT image of sample of rock.

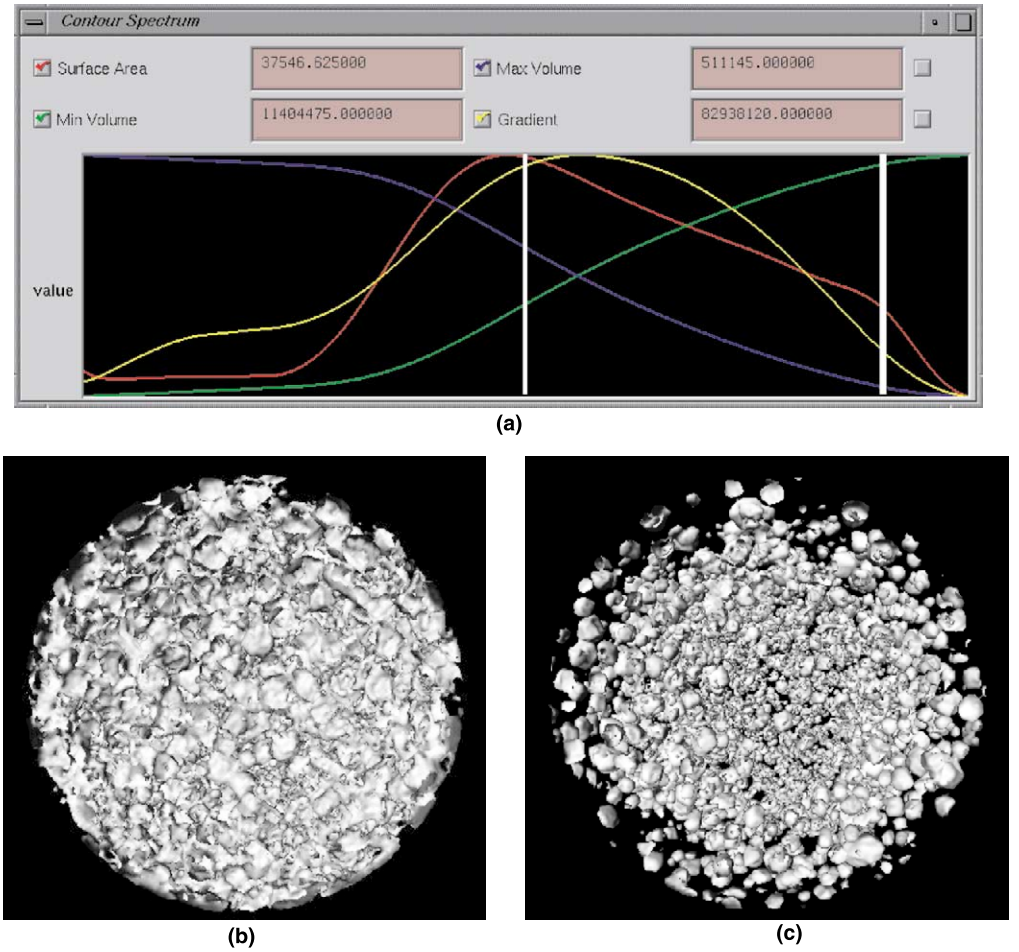

Fig. 3. (a) Contour Spectrum for the rock sample of Fig. 2. (b) and (c) Segmented images for two different choices of the threshold parameter.

As an example, we consider a rock sample whose CT image is shown in Fig. 2. Fig. 3(a) shows the Contour Spectrum for this sample, with the blue line representing the variation of the volume fraction with the threshold parameter. Finally, in Figs. 3(b) and (c), we show the resulting segmented images for two different choices of the threshold parameter. As is seen from these figures, an arbitrary selection of the threshold parameter can result in a highly inaccurate picture of the microstructure.

3.3. Mesh generation

The final step in using the original CT image is to generate a mesh on which computations can be performed. We now discuss the generation of 2-D meshes of quadrilateral elements for the case of two-phase composites with cylindrical (circular) inclusions embedded in a matrix material. Mesh generation using triangles for more general inclusions has been performed but will not be considered here. For the purpose of the present discussion, we assume that the centers and the radii of the inclusions have been extracted from the segmented image of the specimen.

The main steps in the mesh generation algorithm are as follows:

1. Construct the weighted Voronoi diagram of centers of the circles, with the weight proportional to radius.
2. Merge short edges of the Voronoi diagram based on user-specified threshold. If this leads to an intersection between an edge and a circle, the operation is not performed.

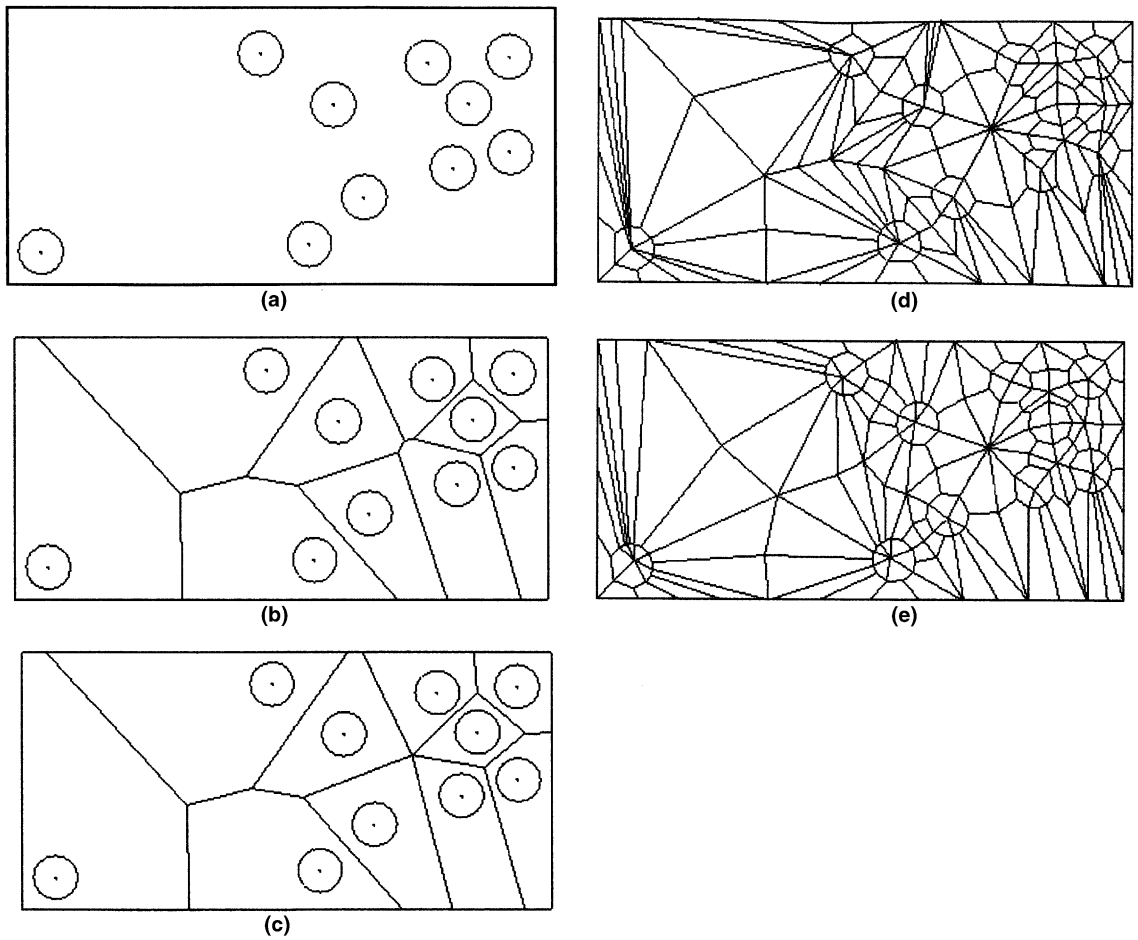

Fig. 4. Meshing algorithm: (a) original configuration of the inclusions, (b) weighted Voronoi diagram for this configuration, (c) Voronoi diagram after removal of short edges, (d) initial mesh, and (e) mesh after five iterations of centroid smoothing.

3. Divide faces of Voronoi cells into n pieces (n is user-specified) by introducing vertices (nodes) on the faces. If a face is shared, this division must be unique.
4. Connect centers of circles to the vertices on the faces, leading to a collection of super-triangles. Each such super-triangle is divided into a quadrilateral and a triangle by the presence of the circle. Optionally, additional division can be performed in the radial direction.
5. Subdivide each triangle into three quadrilaterals.
6. Smooth the mesh using, say, centroid smoothing, wherein an internal node is relocated to the geometric center, or centroid, of the polygon comprised of the elements containing the internal node.

In Fig. 4, some of the steps in the algorithm are illustrated for a simple case. More involved example problems employing the above algorithm will be presented later. It should be noted that the approach described here is not related to the VCFEM of Ghosh and Moorthy (e.g., [9]). Here, the Voronoi cells are not finite elements; they are partitions that encapsulate inclusions and provide a geometric description of needed for automatic meshing. These meshes are adapted using a parallel hp adaptive finite element system discussed in Section 6.

4. Homogenization: determination of effective properties

The term *homogenization*, as used here, refers to processes by which the micromechanical properties of heterogeneous materials are averaged, smeared out over larger scales, so that properties of a homogenized

material are obtained that are, "effectively" those that would be experienced in macroscopic characterizations of material properties. A large body of work exists on this subject and the underlying mathematical theory, and we refer to standard references for full details: see, for example, [5,16,28] or for an engineering-oriented treatment, [6].

4.1. Asymptotic homogenization theory

Much of the classical homogenization theory is concerned with the abstract situation in which the microstructure (the array of coefficients in the governing equations) is periodic with period ϵ. The domain Ω is assumed to be composed of a periodic lattice of cells $Y_\epsilon \subset \mathbb{R}^N$, each cell being the image of a unit cell Y under a dilatation $\mathbf{x} = \epsilon\mathbf{y}$ and a translation. The displacement, strain, and stress fields are then expressed as asymptotic expansions:

$$\begin{aligned}
\mathbf{u}^\epsilon(\mathbf{x},\mathbf{y}) &= \mathbf{u}^0(\mathbf{x}) + \epsilon\mathbf{u}^1(\mathbf{x},\mathbf{y}) + \cdots,\\
\boldsymbol{\varepsilon}^\epsilon(\mathbf{x},\mathbf{y}) &= \boldsymbol{\varepsilon}^0(\mathbf{x},\mathbf{y}) + \epsilon\boldsymbol{\varepsilon}^1(\mathbf{x},\mathbf{y}) + \cdots,\\
\boldsymbol{\sigma}^\epsilon(\mathbf{x},\mathbf{y}) &= \boldsymbol{\sigma}^0(\mathbf{x},\mathbf{y}) + \epsilon\boldsymbol{\sigma}^1(\mathbf{x},\mathbf{y}) + \cdots,
\end{aligned} \tag{13}$$

where $\mathbf{x}$ is the macro-coordinate of a point in Ω and $\mathbf{y}$ is the microcoordinate, $\mathbf{y} = \mathbf{x}/\epsilon$. Here, the superscript ϵ is used to emphasize the dependence of the fields on the size of the cell. Also, where necessary, the subscripts x and y are used to denote differentiation with respect to the macro and microcoordinates, respectively. The expansions above are introduced into the governing equations (1) and one finds that, on the macroscale, the macrostress equilibrium equation is given by

$$-\mathrm{div}_x\langle\boldsymbol{\sigma}^0\rangle(\mathbf{x}) = \mathbf{f}(\mathbf{x}), \tag{14}$$

where $\langle\cdot\rangle$ denotes the unit cell average,

$$\langle\cdot\rangle = \frac{1}{|Y|}\int_Y (\cdot)\,\mathrm{d}\mathbf{y} \tag{15}$$

and

$$\langle\boldsymbol{\sigma}^0\rangle = \mathbf{E}^0\langle\boldsymbol{\varepsilon}^0\rangle, \tag{16}$$

where $\mathbf{E}^0$ is the *effective* or *homogenized* elasticity tensor. It can be shown (e.g., [28]) that

$$E^0_{ijmn} = \langle E_{ijkl}(\mathbf{y})(\delta_{km}\delta_{ln} + \varepsilon_{kly}(\boldsymbol{\chi}^{mn}(\mathbf{y})))\rangle, \tag{17}$$

$1 \leqslant i,j,k,l,m,n \leqslant N$, $\mathbf{y} \in Y$, and $\boldsymbol{\chi}^{mn}$ is a symmetric array of N^2 vector functions of the microscale coordinate $\mathbf{y}$ which are solutions of the following weak BVP:

$$\text{Find } \boldsymbol{\chi}^{mn} \in \mathbf{V}_Y \text{ such that } \langle\boldsymbol{\chi}^{mn}\rangle = 0,\ \mathscr{B}_Y(\boldsymbol{\chi}^{mn},\mathbf{v}) = \mathscr{F}_Y(\mathbf{v})\ \forall\mathbf{v} \in \mathbf{V}_Y, \tag{18}$$

where

$$\mathscr{B}_Y(\boldsymbol{\chi}^{mn},\mathbf{v}) \overset{\text{def}}{=} \int_Y \mathbf{V}_y\mathbf{v} : \mathbf{E}\mathbf{V}_y\boldsymbol{\chi}^{mn}\,\mathrm{d}\mathbf{y}, \quad \mathscr{F}_Y(\mathbf{v}) \overset{\text{def}}{=} -\int_Y E_{ijmn}\frac{\partial v_j}{\partial y_i}\,\mathrm{d}\mathbf{y} \tag{19}$$

and $\mathbf{V}_Y$ is the space of locally H^1 periodic vector valued functions defined on the unit cell Y

$$\mathbf{V}_Y \overset{\text{def}}{=} \left\{\mathbf{v} : \mathbf{v} \in \mathbf{H}^1_{\text{loc}}(\mathbb{R}^N),\ v_i Y - \text{periodic}\right\}. \tag{20}$$

Thus, to determine the effective properties, we solve (18) for $\boldsymbol{\chi}^{mn}$ and then calculate the effective elasticity tensor $\mathbf{E}^0$ using (17).

4.2. Other methods for defining effective properties

Another popular method for defining effective properties of composite materials is based on the notion of RVEs: samples of the heterogeneous material which are (a) larger than typical microscale features, such as fiber diameters, and smaller than the characteristic length of the body itself, and (b) exhibit properties "representative" of the material as a whole. In this approach, no periodicity of microstructure is assumed. However, the material is assumed to be statistically homogeneous: meaning "all global geometrical characteristics such as volume fractions, two-point correlations are the same in any RVE, irrespective of its position"; see [12] and the references cited therein.

The homogenized elasticity tensor is computed as follows: the RVE, also denoted Y, is subjected to either

- displacement boundary conditions of the type

$$\mathbf{u} = \bar{\boldsymbol{\varepsilon}} \cdot \mathbf{y} \quad \text{on } \partial Y, \tag{21}$$

  where $\bar{\boldsymbol{\varepsilon}}$ is a constant prescribed strain tensor or
- traction boundary conditions of the type

$$\mathbf{t} = \bar{\boldsymbol{\sigma}} \cdot \mathbf{n} \quad \text{on } \partial Y, \tag{22}$$

  where $\bar{\boldsymbol{\sigma}}$ is a constant prescribed stress tensor.

Such boundary conditions are referred to as "uniform" boundary conditions in literature. Then, the effective elasticity tensor $\mathbf{E}^0$ is defined by relating the RVE-average of the stress field to the RVE-average of the strain field,

$$\langle \boldsymbol{\sigma} \rangle = \mathbf{E}^0 \langle \boldsymbol{\varepsilon} \rangle. \tag{23}$$

This, of course, implies that the equations of elasticity have to be solved on the RVE, using a numerical method such as the finite element method, in order to compute the effective properties.

An equivalent definition of effective properties of certain composite materials can be given in terms of the strain and stress energy of the RVE. Using these energy expressions and certain extremum principles, Hashin and Shtrikman obtained upper and lower bounds on the effective properties of a composite material with isotropic phases [13,14].

4.3. Current implementation

In our approach, the "unit cell" Y is determined by sampling the microstructure using the imaging process described in the previous section. The cell samples are meshed using the procedures described earlier. Problem (18) is then solved on Y, subject either to periodic or uniform boundary conditions, using an adaptive hp finite element method, described in Section 6. In some cases, we choose to employ the Hashin–Shtrikman bounds. The process also admits a statistical characterization of properties by using the sampling data to obtain statistical averages as in [2]. We note, once again, that the calculation of such effective properties represents only a step in the larger algorithm. While the rate of convergence to results exhibiting the targeted accuracy and the size of the domain of influence will depend on the choice of $\mathbf{E}^0$ (a point discussed in more detail in Section 7), the use of finely tuned estimates of effective properties is not necessary in our approach.

5. Error estimation and adaptive modeling: the GOALS algorithm

In this section, we review the major results regarding modeling error estimation and adaptive modeling presented in [24]. First, we review global energy bounds on the modeling error $\mathbf{e}^0$. Next, bounds on the modeling error in local quantities of interest are briefly discussed. This is followed by a review of the GOALS algorithm [24], a procedure for delivering accurate values of quantities of interest.

5.1. Energy error estimates

Let

$$\mathscr{I}_0 = (\mathbf{I} - \mathbf{E}^{-1}\mathbf{E}^0), \tag{24}$$

where $\mathbf{I}$ is the identity tensor. Next, for $\mathbf{g} \in \mathbf{V}(\Omega)$, define the associated linear *residual functional* $\mathscr{R}_{\mathbf{g}} : \mathbf{V}(\Omega) \to \mathbb{R}$,

$$\mathscr{R}_{\mathbf{g}}(\mathbf{v}) = -\int_\Omega \nabla\mathbf{v} : \mathbf{E}\mathscr{I}_0\nabla\mathbf{g}\,d\mathbf{x}, \quad \mathbf{v} \in \mathbf{V}(\Omega). \tag{25}$$

Finally, define the energy norm of an admissible function $\mathbf{v} \in \mathbf{V}(\Omega)$,

$$\|\mathbf{v}\|_{E(\Omega)} \stackrel{\text{def}}{=} \sqrt{\mathscr{B}_\Omega(\mathbf{v},\mathbf{v})}, \tag{26}$$

where $\mathscr{B}_\Omega(\cdot,\cdot)$ is the bilinear form defined in (7).

Theorem 5.1. *Let* $\mathbf{u}$ *and* $\mathbf{u}^0$ *be the solutions to problems* (5) *and* (9), *respectively. Then the following holds*:

$$\zeta_{\text{low}} \leqslant \|\mathbf{e}^0\|_{E(\Omega)} = \|\mathbf{u} - \mathbf{u}^0\|_{E(\Omega)} \leqslant \zeta_{\text{upp}}, \tag{27}$$

where

$$\zeta_{\text{low}} \stackrel{\text{def}}{=} \frac{|\mathscr{R}_{\mathbf{u}^0}(\mathbf{u}^0)|}{\|\mathbf{u}^0\|_{E(\Omega)}}, \quad \zeta_{\text{upp}} \stackrel{\text{def}}{=} \left\{ \int_\Omega \mathscr{I}_0\nabla\mathbf{u}^0 : \mathbf{E}\mathscr{I}_0\nabla\mathbf{u}^0\,d\mathbf{x} \right\}^{1/2}. \tag{28}$$

For proofs, see [23,31].

5.2. Local error estimates

Let L be a quantity of interest that is characterized by a continuous linear functional $\mathbf{V}(\Omega)$, $L \in \mathbf{V}'(\Omega)$. The problem

$$\boxed{\text{Find } \mathbf{w} \in \mathbf{V}(\Omega) \text{ such that } \mathscr{B}_\Omega(\mathbf{v},\mathbf{w}) = L(\mathbf{v}) \ \forall \mathbf{v} \in \mathbf{V}(\Omega)} \tag{29}$$

is referred to as the *adjoint fine-scale problem*. The solution $\mathbf{w}$ to the adjoint fine-scale problem is termed the *fine-scale influence function*. The homogenized version of this problem is referred to as the *adjoint homogenized problem* and reads

$$\boxed{\text{Find } \mathbf{w}^0 \in \mathbf{V}(\Omega) \text{ such that } \mathscr{B}^0_\Omega(\mathbf{v},\mathbf{w}^0) = L(\mathbf{v}) \ \forall \mathbf{v} \in \mathbf{V}(\Omega).} \tag{30}$$

The solution to this problem is the *homogenized influence function*. In what follows, we sometimes refer to the problems (5) and (9) as the *primal fine-scale problem* and *primal homogenized problem*, respectively. Functions $\mathbf{w}$ and $\mathbf{w}^0$ exist and are uniquely defined. The modeling error in the influence function is given by

$$\bar{\mathbf{e}}^0 \stackrel{\text{def}}{=} \mathbf{w} - \mathbf{w}^0. \tag{31}$$

Also, $\bar{\mathbf{e}}^0$ satisfies the following relationship:

$$\bar{\zeta}_{\text{low}} \leqslant \|\bar{\mathbf{e}}^0\|_{E(\Omega)} = \|\mathbf{w} - \mathbf{w}^0\|_{E(\Omega)} \leqslant \bar{\zeta}_{\text{upp}}, \tag{32}$$

where

$$\bar{\zeta}_{\text{low}} \stackrel{\text{def}}{=} \frac{|\mathscr{R}_{\mathbf{w}^0}(\mathbf{w}^0)|}{\|\mathbf{w}^0\|_{E(\Omega)}}, \quad \bar{\zeta}_{\text{upp}} \stackrel{\text{def}}{=} \left\{ \int_\Omega \mathscr{I}_0\nabla\mathbf{w}^0 : \mathbf{E}\mathscr{I}_0\nabla\mathbf{w}^0\,d\mathbf{x} \right\}^{1/2}. \tag{33}$$

We now state the main result on the estimation of modeling error in quantities of interest.

Theorem 5.2. *Let* $\mathbf{u}^0$ *and* $\mathbf{w}^0$ *be the solutions to problems* (9) *and* (30), *respectively. Then*

$$\eta_{\text{low}} \leqslant L(\mathbf{e}^0) \leqslant \eta_{\text{upp}}, \tag{34}$$

where

$$\eta_{\text{low}} \stackrel{\text{def}}{=} \frac{1}{4}(\eta_{\text{low}}^{+})^2 - \frac{1}{4}(\eta_{\text{upp}}^{-})^2 + \mathscr{R}_{\mathbf{u}^0}(\mathbf{w}^0), \tag{35}$$

$$\eta_{\text{upp}} \stackrel{\text{def}}{=} \frac{1}{4}(\eta_{\text{upp}}^{+})^2 - \frac{1}{4}(\eta_{\text{low}}^{-})^2 + \mathscr{R}_{\mathbf{u}^0}(\mathbf{w}^0) \tag{36}$$

with arbitrary $s \in \mathbb{R}^+$,

$$\eta_{\text{upp}}^{\pm} \stackrel{\text{def}}{=} \sqrt{s^2\zeta_{\text{upp}}^2 \pm 2\int_{\Omega} \mathscr{I}_0\nabla\mathbf{u}^0 : \mathbf{E}\,\mathscr{I}_0\nabla\mathbf{w}^0\,\mathrm{d}\mathbf{x} + s^{-2}\bar{\zeta}_{\text{upp}}^2} \tag{37}$$

and

$$\eta_{\text{low}}^{\pm} \stackrel{\text{def}}{=} \frac{|\mathscr{R}_{s\mathbf{u}^0 \pm s^{-1}\mathbf{w}^0}(\mathbf{u}^0 + \theta^{\pm}\mathbf{w}^0)|}{\|\mathbf{u}^0 + \theta^{\pm}\mathbf{w}^0\|_{E(\Omega)}}, \tag{38}$$

where ζ_{upp} *and* $\bar{\zeta}_{\text{upp}}$ *are defined by* (28) *and* (33), *respectively, and* $\theta^{\pm}$ *is given by*

$$\theta^{\pm} = \frac{\mathscr{B}_{\Omega}(\mathbf{u}^0,\mathbf{w}^0)\mathscr{R}_{\mathbf{u}^0}(s\mathbf{u}^0 \pm s^{-1}\mathbf{w}^0) - \mathscr{B}_{\Omega}(\mathbf{u}^0,\mathbf{u}^0)\mathscr{R}_{\mathbf{w}^0}(s\mathbf{u}^0 \pm s^{-1}\mathbf{w}^0)}{\mathscr{B}_{\Omega}(\mathbf{u}^0,\mathbf{w}^0)\mathscr{R}_{\mathbf{w}^0}(s\mathbf{u}^0 \pm s^{-1}\mathbf{w}^0) - \mathscr{B}_{\Omega}(\mathbf{w}^0,\mathbf{w}^0)\mathscr{R}_{\mathbf{u}^0}(s\mathbf{u}^0 \pm s^{-1}\mathbf{w}^0)}. \tag{39}$$

See [23] for the proof. The scalar parameter s is a scaling factor and its optimal value is $s^* = \sqrt{\bar{\zeta}_{\text{upp}}/\zeta_{\text{upp}}}$. Also, in our numerical experiments, we employ the following *estimate* of the modeling error in the quantity of interest:

$$L(\mathbf{e}^0) \approx \eta_{\text{est}} \stackrel{\text{def}}{=} \frac{1}{4}(\eta_{\text{upp}}^{+})^2 - \frac{1}{4}(\eta_{\text{upp}}^{-})^2 + \mathscr{R}_{\mathbf{u}^0}(\mathbf{w}^0). \tag{40}$$

5.3. Definition of the local fine-scale problem

For the purpose of simplicity, we assume that the quantity of interest L is a functional of the form

$$L(\mathbf{v}) = \int_{\omega} l(\mathbf{v})\,\mathrm{d}\mathbf{x}, \tag{41}$$

where l is a linear map $l : \mathbf{V}(\Omega) \to L^1_{\text{loc}}(\Omega)$. Here, ω is some subset of the domain Ω. Functionals of other types can be accommodated very easily in our approach. Let Ω_L be a subset of the domain Ω that contains ω: $\omega \subset \Omega_L$. We shall refer to Ω_L as the functional's "domain of influence", and it's determination will be discussed shortly.

In order to define the local fine-scale problem on Ω_L, we introduce some notation. Let

$$\Gamma_{L_t} \stackrel{\text{def}}{=} \partial\Omega_L \cap \Gamma_t, \quad \Gamma_{L_u} \stackrel{\text{def}}{=} \partial\Omega_L \setminus \Gamma_{L_t}. \tag{42}$$

Define the local function space on Ω_L as

$$\mathbf{V}(\Omega_L) = \left\{\mathbf{v} \in \mathbf{V}(\Omega),\ \mathbf{v} = \mathbf{0} \text{ on } \Omega \setminus \overline{\Omega_L},\ \mathbf{v}|_{\Gamma_{L_u}} = \mathbf{0}\right\}. \tag{43}$$

Next, an extension operator $\mathscr{E}_L : \mathbf{V}(\Omega_L) \to \mathbf{V}(\Omega)$ is introduced, defined by:

$$\mathbf{v}_L \in \mathbf{V}(\Omega_L), \quad \mathscr{E}_L(\mathbf{v}_L) = \mathbf{v} \text{ such that } \mathbf{v}|_{\Omega_L} = \mathbf{v}_L,\ \mathbf{v}|_{\Omega\setminus\Omega_L} = \mathbf{0}. \tag{44}$$

The restriction of the homogenized solution $\mathbf{u}^0$ to the domain of influence Ω_L is defined as $\mathbf{u}_L^0 : \mathbf{u}_L^0 \stackrel{\text{def}}{=} \mathbf{u}^0|_{\Omega_L}$.Then, the following weak BVP is referred to as the *local fine-scale problem*:

$$\boxed{\text{Find } \tilde{\mathbf{u}}_L \in \{\mathbf{u}_L^0\} + \mathbf{V}(\Omega_L) \text{ such that } \mathscr{B}_L(\tilde{\mathbf{u}}_L, \mathbf{v}_L) = \mathscr{F}_L(\mathbf{v}_L)\ \forall \mathbf{v}_L \in \mathbf{V}(\Omega_L),} \tag{45}$$

where the bilinear and linear forms are defined as

$$\mathscr{B}_L(\tilde{\mathbf{u}}_L, \mathbf{v}_L) \stackrel{\text{def}}{=} \int_{\Omega_L} \nabla \mathbf{v}_L : \mathbf{E}\nabla \tilde{\mathbf{u}}_L \, d\mathbf{x} \tag{46}$$

and

$$\mathscr{F}_L(\mathbf{v}_L) \stackrel{\text{def}}{=} \int_{\Omega_L} \mathbf{f} \cdot \mathbf{v}_L \, d\mathbf{x} + \int_{\Gamma_{L_t}} \mathbf{t} \cdot \mathbf{v}_L \, d\mathbf{s}, \tag{47}$$

respectively. Thus, $\tilde{\mathbf{u}}_L$ is a perturbation to the homogenized solution $\mathbf{u}^0$ on Ω_L that takes into account the fine-scale microstructure. It equals the primal homogenized solution $\mathbf{u}^0$ on the Γ_{L_u} portion of its boundary. Using the extension operator $\mathscr{E}_k$, we define the *locally enhanced* function $\tilde{\mathbf{u}} \in \mathbf{V}(\Omega)$ as:

$$\tilde{\mathbf{u}} \stackrel{\text{def}}{=} \mathbf{u}^0 + \mathscr{E}_L(\tilde{\mathbf{u}}_L - \mathbf{u}_L^0). \tag{48}$$

Finally, it is noted that the modeling error $\mathbf{u} - \tilde{\mathbf{u}}$ can also be estimated – both globally in the energy norm, and locally in the quantity of interest – using the results presented in [24].

5.4. Modeling error estimates for perforated materials

The results presented in Theorems 5.1 and 5.2 are applicable to n-phase heterogeneous materials, but not to perforated domains. The main difference between these two cases is that in the former, it is the elasticity tensor that is homogenized or smeared out, whereas in the latter, the domain also gets smeared out. Thus, the fine-scale and homogenized problems are posed on different domains, and new error estimates need to be developed. Here, we merely state the main result on estimating the modeling error in the energy norm for perforated domains; see [30] for the proof.

The perforated body, shown in Fig. 5(a), is assumed to occupy an open bounded domain $\Omega \subset \mathbb{R}^N,\ N = 2, 3$. The boundaries of the voids inside the body are denoted $\gamma_i, 1 \leqslant i \leqslant N_v$. The following assumptions are made about the voids:

- the voids are traction-free;
- the voids are sufficiently smooth, i.e., the domain Ω is connected, and the Korn's inequality and the standard trace theorem for H^1 functions on polygonal domains still hold; and
- the voids do not intersect the outer boundary $\partial\Omega$.

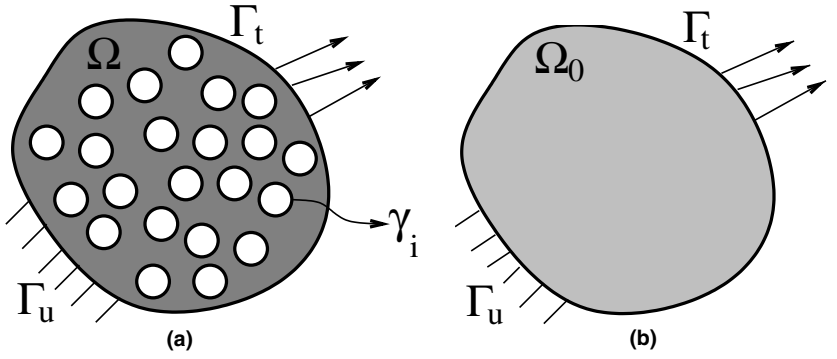

Fig. 5. Schematic of (a) a perforated domain, and (b) the homogenized model of the perforated domain.

It is also assumed that the material is linearly elastic and that the elasticity tensor E_{ijkl} obeys standard ellipticity and symmetry conditions. Under the stated assumptions, the fine-scale displacement field $\mathbf{u}$ is the solution to following fine-scale problem:

$$\boxed{\text{Find } \mathbf{u} \in \mathbf{V}(\Omega) \text{ such that } \mathscr{B}_{\Omega}(\mathbf{u},\mathbf{v}) = \mathscr{F}_{\Omega}(\mathbf{v}) \ \forall \mathbf{v} \in \mathbf{V}(\Omega),} \tag{49}$$

where $\mathscr{B}_{\Omega}(\cdot,\cdot), \mathscr{F}_{\Omega}(\cdot)$ and $\mathbf{V}(\Omega)$ are as defined in Section 2.5.

In the homogenized version of the above problem, the domain Ω is replaced by a domain without voids, denoted by Ω_0 (see Fig. 5(b)). The boundary conditions on Γ_u and Γ_t remain unchanged. To account for the smearing out of the voids, the material moduli $\mathbf{E}$ are replaced by moduli $\mathbf{E}^0$, representing a softening of the material. Then, the *homogenized solution* $\mathbf{u}^0$ is the solution to the following *homogenized problem*:

$$\boxed{\text{Find } \mathbf{u}^0 \in \mathbf{V}(\Omega_0) \text{ such that } \mathscr{B}^0_{\Omega_0}(\mathbf{u}^0,\mathbf{v}) = \mathscr{F}^0_{\Omega_0}(\mathbf{v}) \ \forall \mathbf{v} \in \mathbf{V}(\Omega_0).} \tag{50}$$

The homogenized bilinear and linear forms are given by

$$\mathscr{B}^0_{\Omega_0}(\mathbf{u}^0,\mathbf{v}) \stackrel{\text{def}}{=} \int_{\Omega_0} \nabla\mathbf{v} : \mathbf{E}^0 \nabla\mathbf{u}^0 \,\mathrm{d}\mathbf{x}, \quad \mathscr{F}^0_{\Omega_0}(\mathbf{v}) \stackrel{\text{def}}{=} \int_{\Omega_0} \mathbf{f}\cdot\mathbf{v}\,\mathrm{d}\mathbf{x} + \int_{\Gamma_t} \mathbf{t}\cdot\mathbf{v}\,\mathrm{d}\mathbf{s}, \tag{51}$$

and the space of admissible functions is defined as

$$\mathbf{V}(\Omega_0) \stackrel{\text{def}}{=} \left\{ \mathbf{v} \in \left(H^1(\Omega_0)\right)^N : \mathbf{v}|_{\Gamma_u} = \mathbf{0} \right\}. \tag{52}$$

Since the fine-scale solution $\mathbf{u} : \Omega \to \mathbb{R}^N$ and the homogenized solution $\mathbf{u}^0 : \Omega_0 \to \mathbb{R}^N$ are defined on different domains, we work with the restriction of the homogenized solution to the perforated domain, also denoted $\mathbf{u}^0$. Then, the modeling error $\mathbf{e}^0 : \Omega \to \mathbb{R}^N$ is defined as

$$\mathbf{e}^0 \stackrel{\text{def}}{=} \mathbf{u} - \mathbf{u}^0. \tag{53}$$

Let the *residual functional* $\mathscr{R}_{\mathbf{g}} : \mathbf{V}(\Omega) \to \mathbb{R}$, for $\mathbf{g}, \mathbf{v} \in \mathbf{V}(\Omega)$, be redefined as follows:

$$\mathscr{R}_{\mathbf{g}}(\mathbf{v}) \stackrel{\text{def}}{=} -\int_{\Omega} \nabla\mathbf{v} : \mathbf{E}\mathscr{I}_0\nabla\mathbf{g}\,\mathrm{d}\mathbf{x} - \sum_{i=1}^{N_v} \int_{\gamma_i} \mathbf{v}\cdot(\mathbf{E}^0\nabla\mathbf{g}\cdot\mathbf{n})\,\mathrm{d}\mathbf{s}, \tag{54}$$

where $\mathbf{n}$ is the unit outward normal to γ_i.

Theorem 5.3. *Let* $\mathbf{u}$ *and* $\mathbf{u}^0$ *be as defined above. Then the following holds*:

$$\zeta_{\text{low}} \leqslant \|\mathbf{e}^0\|_{E(\Omega)} = \|\mathbf{u}-\mathbf{u}^0\|_{E(\Omega)} \leqslant \zeta_{\text{upp}} + C\sum_{i=1}^{N_v} \kappa_i, \tag{55}$$

where

$$\zeta_{\text{low}} \stackrel{\text{def}}{=} \frac{|\mathscr{R}_{\mathbf{u}^0}(\mathbf{u}^0)|}{\|\mathbf{u}^0\|_{E(\Omega)}} \tag{56}$$

and

$$\zeta_{\text{upp}} \stackrel{\text{def}}{=} \sqrt{\int_{\Omega} \mathscr{I}_0\nabla\mathbf{u}^0 : \mathbf{E}\mathscr{I}_0\nabla\mathbf{u}^0\,\mathrm{d}\mathbf{x}}, \quad \kappa_i \stackrel{\text{def}}{=} \|\mathbf{E}^0\nabla\mathbf{u}^0\cdot\mathbf{n}\|_{\mathbf{L}^2(\gamma_i)}. \tag{57}$$

The constant C *depends on the boundaries of the voids inside* Ω *and the elasticity tensor* $\mathbf{E}$.

With the energy bounds in hand, bounds on the modeling error in quantities of interest can easily be obtained, as described in our companion paper [24].

5.5. The GOALS algorithm

The GOALS algorithm provides an adaptive procedure for accurately computing a quantity of interest $L(\mathbf{u})$ by determining the size of its domain of influence. For this purpose, we introduce a partition $\mathscr{P}$ of the domain Ω into cells Θ_k, $1 \leqslant k \leqslant N(\mathscr{P})$, where $N(\mathscr{P})$ is the total number of cells in the partition. The following modeling *error indicators* are used in the GOALS algorithm:

$$\begin{aligned} \zeta_{k,\mathrm{upp}} &\stackrel{\mathrm{def}}{=} \left\{ \int_{\Theta_k} \mathscr{I}_0 \nabla \mathbf{u}^0 : \mathbf{E}\, \mathscr{I}_0 \nabla \mathbf{u}^0 \, \mathrm{d}\mathbf{x} \right\}^{1/2}, \\ \bar{\zeta}_{k,\mathrm{upp}} &\stackrel{\mathrm{def}}{=} \left\{ \int_{\Theta_k} \mathscr{I}_0 \nabla \mathbf{w}^0 : \mathbf{E}\, \mathscr{I}_0 \nabla \mathbf{w}^0 \, \mathrm{d}\mathbf{x} \right\}^{1/2} \end{aligned} \tag{58}$$

and

$$\beta_k \stackrel{\mathrm{def}}{=} \zeta_{k,\mathrm{upp}} \bar{\zeta}_{k,\mathrm{upp}} + \zeta_{k,\mathrm{upp}} \|\mathbf{w}^0\|_{E(\Theta_k)}. \tag{59}$$

The indicators $\zeta_{k,\mathrm{upp}}$ and $\bar{\zeta}_{k,\mathrm{upp}}$ are contributions of a cell to the modeling errors estimates ζ_{upp} and $\bar{\zeta}_{\mathrm{upp}}$ (recall (28) and (33)), respectively. The measure β_k is an indicator of the local contribution of a cell to the modeling error in the quantity of interest.

The outline of the GOALS algorithm is as follows:

Step 1. *Initialization*. Given the initial data Ω, Γ_u, Γ_t, $\mathbf{E}$, $\mathbf{f}$ and $\mathbf{t}$, construct a nonoverlapping partition of the domain $\mathscr{P} = \{\Theta_k\}$, $k = 1, 2, \ldots, N(\mathscr{P})$. Specify error tolerance parameters α_{TOL} and δ_{TOL}, $0 < \delta_{\mathrm{TOL}} < 1$.

Step 2. *Homogenization*. Compute the homogenized elasticity tensor $\mathbf{E}^0$. Solve the primal homogenized problem (9) for $\mathbf{u}^0$ and the adjoint homogenized problem (30) for $\mathbf{w}^0$.

Step 3. *Modeling error estimation*. Compute error indicators ζ_k, $\bar{\zeta}_k$ and β_k for $1 \leqslant k \leqslant N(\mathscr{P})$, using (58) and (59). Estimate the modeling error in the quantity of interest using Theorem 3.1. Denote this estimate by η_{est}.

Step 4. *Tolerance test*. If $\eta_{\mathrm{est}} \leqslant \alpha_{\mathrm{TOL}} \times L(\mathbf{u}^0)$, STOP.

Step 5. *Domain of influence*. Determine initial guess for "domain of influence" Ω_L as all the cells that intersect ω, the region over which the quantity of interest is defined

$$\overline{\Omega_L} = \overline{\bigcup_{j \in \mathscr{J}} \Theta_j}\, \mathscr{J} \stackrel{\mathrm{def}}{=} \{ j : \Theta_j \cap \omega \neq \emptyset \}. \tag{60}$$

Compute the quantities $\zeta_L, \bar{\zeta}_L$, and β_L:

$$\zeta_L \stackrel{\mathrm{def}}{=} \left\{ \sum_{k \in \mathscr{J}} \zeta^2_{k,\mathrm{upp}} \right\}^{1/2}, \quad \bar{\zeta}_L \stackrel{\mathrm{def}}{=} \left\{ \sum_{k \in \mathscr{J}} \bar{\zeta}^2_{k,\mathrm{upp}} \right\}^{1/2}, \quad \beta_L \stackrel{\mathrm{def}}{=} \zeta_L \bar{\zeta}_L + \zeta_L \|\mathbf{w}^0\|_{E(\Omega_L)}. \tag{61}$$

Step 6. *Update domain of influence*. Determine the "bad neighbors" of Ω_L, i.e., if $\beta_i > \delta_{\mathrm{TOL}} \times |\Theta_i|/|\Omega_L| \times \beta_L$, mark Θ_i as bad and update Ω_L:

$$\Omega_L \leftarrow \Omega_L \cup \{\text{bad neighbors}\}. \tag{62}$$

Update the quantities $\zeta_L, \bar{\zeta}_L$, and β_L.

Step 7. *Solution of local problem*. Solve local problem (45) on Ω_L for $\tilde{\mathbf{u}}_L$. Construct the locally enhanced solution $\tilde{\mathbf{u}} \in \mathbf{V}(\Omega)$ using (48).

Step 8. *Estimate modeling error*. Estimate the modeling error $L(\mathbf{u} - \tilde{\mathbf{u}})$ and denote the estimate by η_{est}. If $\eta_{\mathrm{est}} \leqslant \alpha_{\mathrm{TOL}} \times L(\tilde{\mathbf{u}})$, STOP. ELSE, GOTO Step 6.

6. Parallel hp adaptive FEM for material modeling

6.1. Computational requirements for adaptive modeling

The adaptive modeling process described in the previous sections requires the solution of three different BVPs: (1) the BVP on the unit cell Y for the computation of the homogenized elasticity tensor $\mathbf{E}^0$, (2) the homogenized primal and adjoint problems for $\mathbf{u}^0$ and $\mathbf{w}^0$, and (3) the local fine-scale problems on domains of influence Ω_L for $\tilde{\mathbf{u}}_L$. Additionally, the primal and adjoint fine-scale problems are sometimes solved for $\mathbf{u}$ and $\mathbf{w}$, respectively, to obtain reference solutions so that the accuracy of the modeling error estimates can be verified and the adaptive modeling procedure validated.

In order to isolate the modeling error, it is necessary to solve these BVPs with very high accuracy. This in turn requires the solution of very large sparse systems of equations. Also, the modeling algorithm imposes certain requirements on the implementation. To list a few:

- Both the global and local error estimates involve the computation of integrals over the domain ω. These integrals have to be computed with high accuracy.
- Boundary conditions for the local fine-scale problems need to be extracted from the homogenized solution.
- In order to handle the output from the meshing code, the representation of element geometry has to be well separated from the approximation shape functions.

6.2. Features of the hp code

With these requirements in mind, a 2-D *parallel* and *adaptive* finite element solver was developed for the implementation of the adaptive modeling procedure. The main features of the code are:

1. *Language*. The code is written in C++ and uses the MPICH version of the message passing interface (MPI) [10,11].
2. *Adaptivity*. Mesh refinement is done using 1-irregular divisions of elements. Hierarchical shape functions are used for p adaptivity. For a discussion of hp adaptive finite elements, see [27].
3. *Parallelism*. The code is designed to run on distributed memory machines. The notion of SFCs is used to perform partitioning of the domain and achieve load-balancing [7,26].
4. *Solution strategy* In the current version, the DOF corresponding to the bubble functions are first eliminated, and the resulting system of equations is solved using either (a) a preconditioned Conjugate Gradient algorithm or (b) the sparse object-oriented linear equations solver (SPOOLES) package, a public domain software [1].
5. *Datastructure*. A Hash table-based datastructure is used for storing element, node and DOF classes. Very general classes have been implemented for storing material and boundary condition data.
6. *Organization, structure and others*. The code is organized as a library-style collection of routines, with the user supplying a few routines that specify the problem parameters. Post-processing is user defined. User-specified integration rules can be used instead of the default integration routines. Additionally, the code is capable of running in batch and interactive modes.

The code has been tested on (a) cluster of PCs running Linux, (b) cluster of SGI workstations running IRIX 6.5 and (c) an IBM SP running AIX 4.1.4.

7. Numerical experiments and examples

In this section, we present several numerical examples that demonstrate both the effectivity of the various estimates as well as the applicability of the adaptive modeling procedure. The first example involves a straight-forward application of the GOALS algorithm to a 2-D composite with a large number of inclusions that are periodically arranged. Next, this exercise is repeated for a 3-D structure with periodically arranged spherical inclusions. Then, in Example 3, we consider a composite material characterized by a graded microstructure. In Example 4, we apply the adaptive modeling algorithm to a perforated domain.

The fifth example involves the fabrication, imaging and adaptive modeling of an epoxy-glass composite and draws upon the different technologies discussed in this paper. Finally, the last example involves the study of a composite wrench with a very large number of inclusions. We present the results of the application of our procedure to this problem, in which the fine-scale information is known only in certain locations.

7.1. Example 1

Our first example consists of a heterogeneous elastic structure that has a periodic microstructure, as shown in Fig. 6. The volume fraction of the inclusions is taken to be 0.5. The material properties are taken to be $E = 100$ GPa, $v = 0.2$ for the matrix material, and $E = 1000$ GPa, $v = 0.2$ for the inclusions.

The goal of the analysis is to predict the average stress σ_{yy} on the inclusion ω. Thus

$$L(\mathbf{v}) = \frac{1}{|\omega|}\int_{\omega} \sigma_{yy}(\mathbf{v})\,\mathrm{d}\mathbf{x}. \tag{63}$$

We remark that $L(\mathbf{e}^0) = L(\mathbf{u}) - L(\mathbf{u}^0)$ is *not* the error in the averaged stress over ω. The σ_{yy}-stress error is

$$\frac{1}{|\omega|}\int_{\omega}\left(E_{22kl}u_{k,l} - E^0_{22kl}u^0_{k,l}\right)\mathrm{d}\mathbf{x} = L(\mathbf{e}^0) + \frac{1}{|\omega|}\int_{\omega} E_{22kl}(\mathscr{I}_0)_{klij}u^0_{i,j}\,\mathrm{d}\mathbf{x}. \tag{64}$$

As the GOALS process progressively adjusts the domain of influence Ω_L to achieve target accuracies, the second term on the right-hand side of (64) vanishes, and $L(\mathbf{u} - \tilde{\mathbf{u}})$ represents the actual stress-average error.

For the purpose of comparison, a reference solution $\mathbf{u}$ is computed on a fine-scale mesh with about 250,000 DOF. The mesh, as well as the SFC partition of the mesh, are shown in Fig. 7. The solution was computed in 340 s on 12 processors of an IBM SP2.

The material is homogenized by solving the unit-cell equations (18) on a square region with a single inclusion. The unit cell and the resulting solutions $\boldsymbol{\chi}^{mn},\ m,n = 1,2$ are shown in Fig. 8.

Next, the homogenized primal and adjoint solutions $\mathbf{u}^0$ and $\mathbf{w}^0$ are determined on a highly refined hp mesh with about 20,000 DOF. The error estimates and indicators are then computed. As suggested by the normalized distribution of the local modeling error indicators β_k, shown in Fig. 9, only local information is needed to predict the quantity of interest accurately. Another observation that can be made is that since the error indicators are virtually negligible in all the cells except those in the vicinity of the quantity of interest, one need compute the indicators – which are essentially integrals involving the homogenized solutions $\mathbf{u}^0$ and $\mathbf{w}^0$, and the fine-scale information $\mathbf{E}$ – only in the neighborhood of the quantity of interest. In

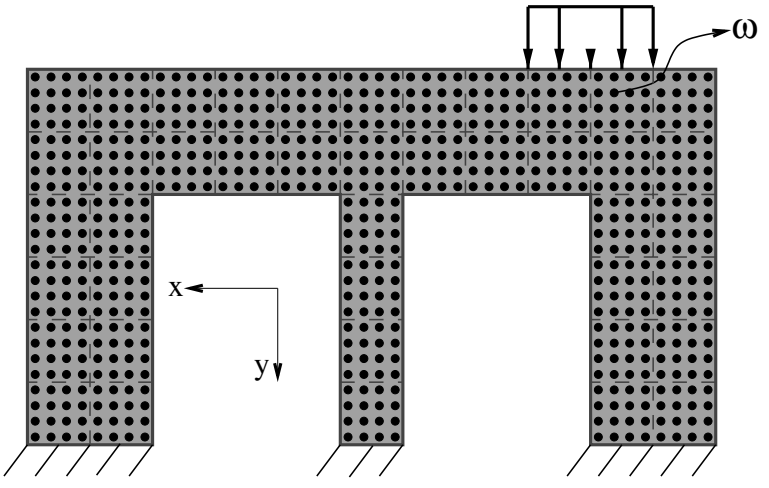

Fig. 6. Example 1: schematic of the problem.

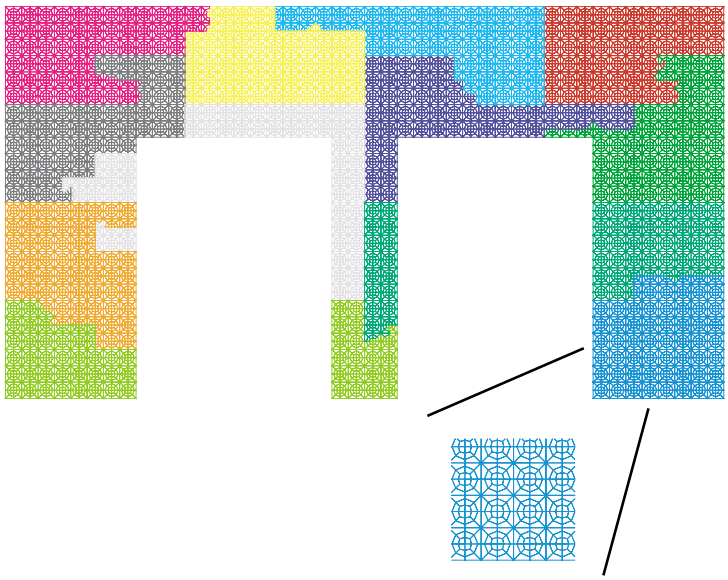

Fig. 7. Example 1: mesh for the fine-scale solution and the partitioning of the problem generated by the SFC. Coloring indicates the processor to which a subdomain belongs.

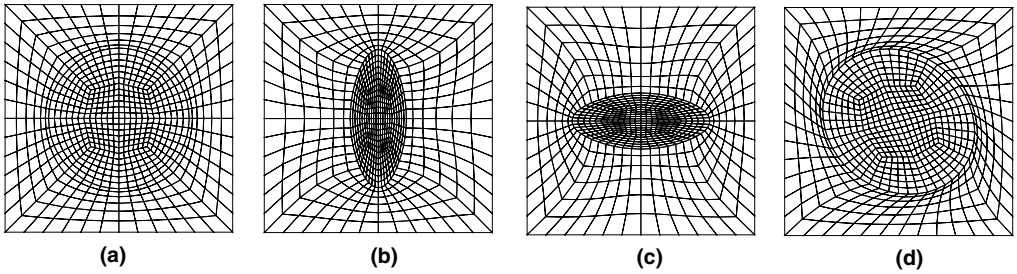

Fig. 8. Example 1: homogenization of a periodic medium: (a) the unit cell and solutions to the periodic BVPs on unit cell shown as mode functions (b) χ^{11}, (c) χ^{22}, and (d) χ^{12}.

Fig. 9. Example 1: normalized distribution of local modeling error indicators β_k.

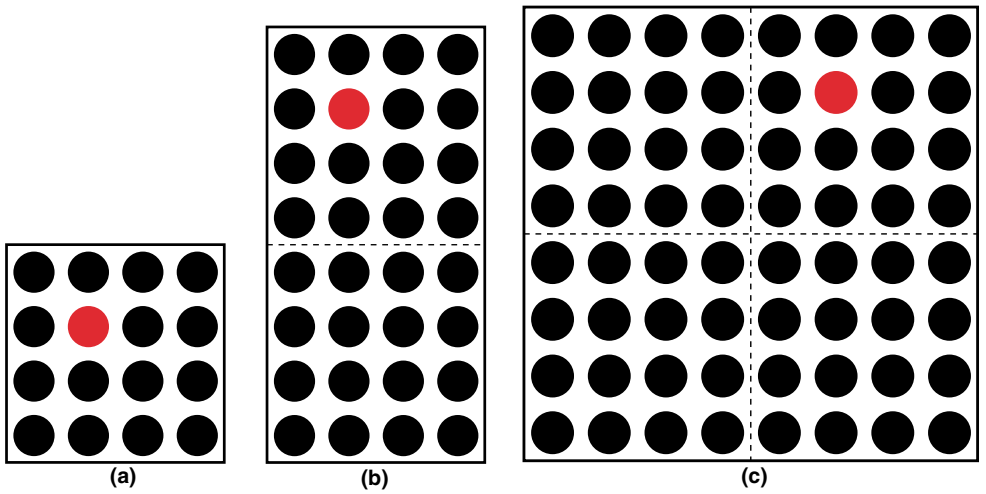

Fig. 10. Example 1: sequence of domains of influence and resulting errors in the predicted quantity of interest. The inclusion of interest is shown in red: (a) $L(\mathbf{u}-\tilde{\mathbf{u}})/L(\mathbf{u}) = 0.199$; (b) $L(\mathbf{u}-\tilde{\mathbf{u}})/L(\mathbf{u}) = 0.120$; (c) $L(\mathbf{u}-\tilde{\mathbf{u}})/L(\mathbf{u}) = 0.010$.

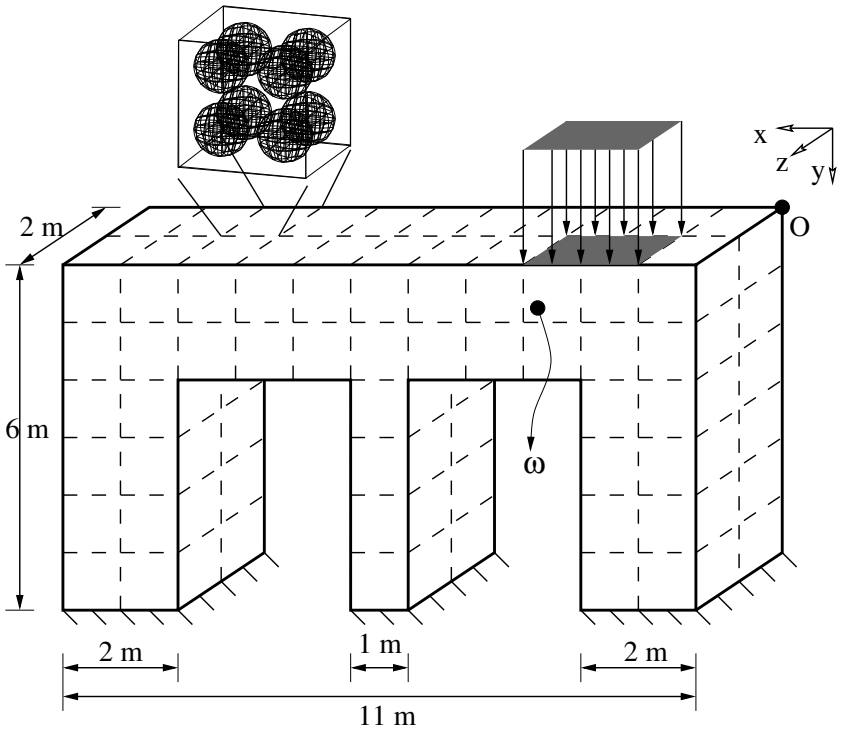

Fig. 11. Schematic of the 3-D problem.

summary, for this example, *the fine-scale information only needs to be known locally* to compute a quantity of interest.

This observation is confirmed by the results of the adaptive procedure, shown in Fig. 10. By iteratively enlarging the size of the domain of influence, we find that the error in the quantity of interest is reduced to 1% in three steps. The number of DOF used to solve the local microscale problem on the final domain of influence shown in Fig. 10(c) was 26,800.

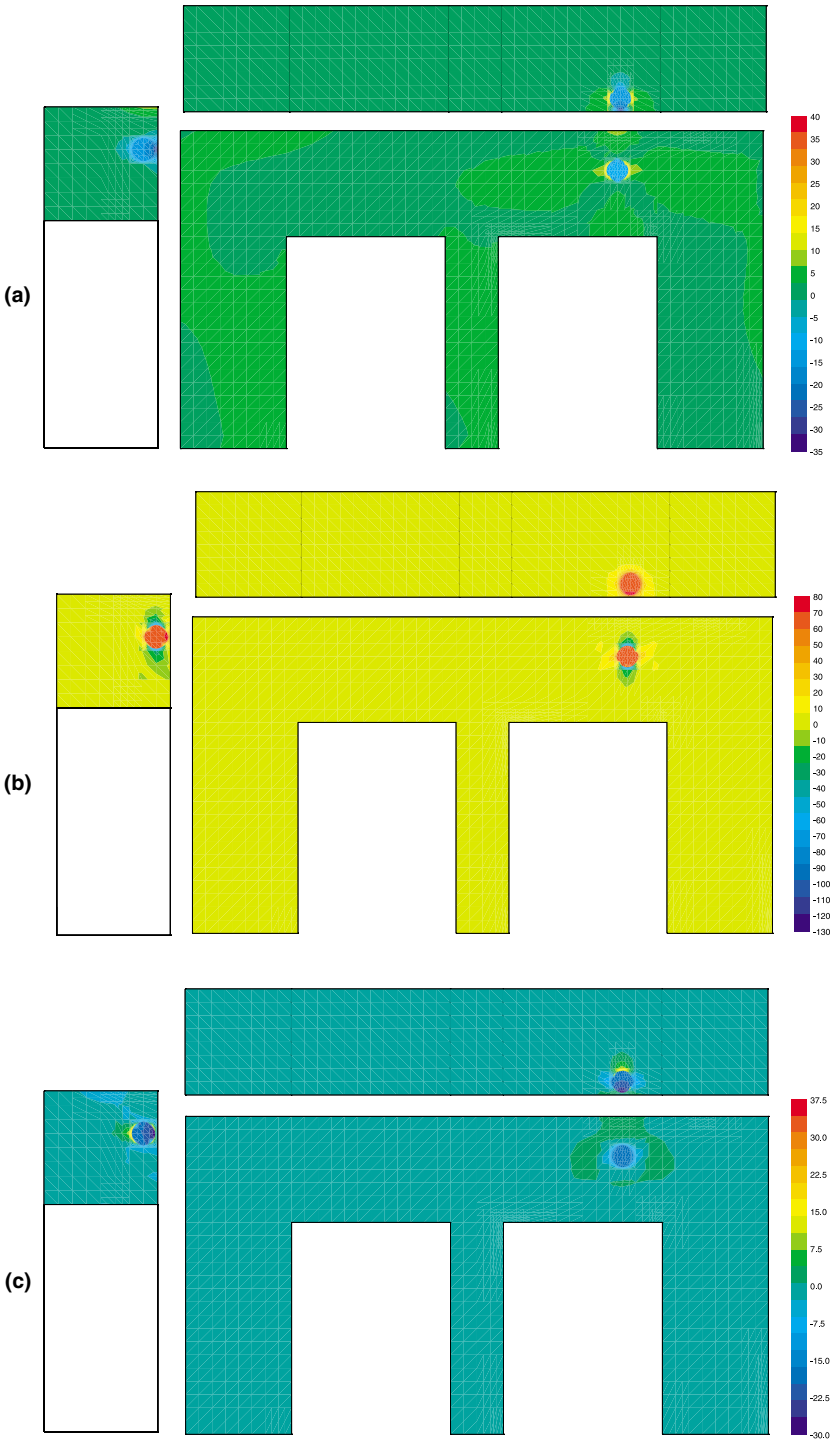

Fig. 12. Example 2: normal components of the strain tensor $\boldsymbol{\varepsilon}(\mathbf{w}^0)$: (a) $\varepsilon_{11}(\mathbf{w}^0)$, (b) $\varepsilon_{22}(\mathbf{w}^0)$, and (c) $\varepsilon_{33}(\mathbf{w}^0)$.

7.2. Example 2

We now study the deformation of a 3-D heterogeneous structure, depicted in Fig. 11. The structure is fixed at the bottom, and has tractions applied on a portion of its boundary. The microstructure in this problem consists of spherical inclusions arranged periodically in a matrix material. The volume fraction of

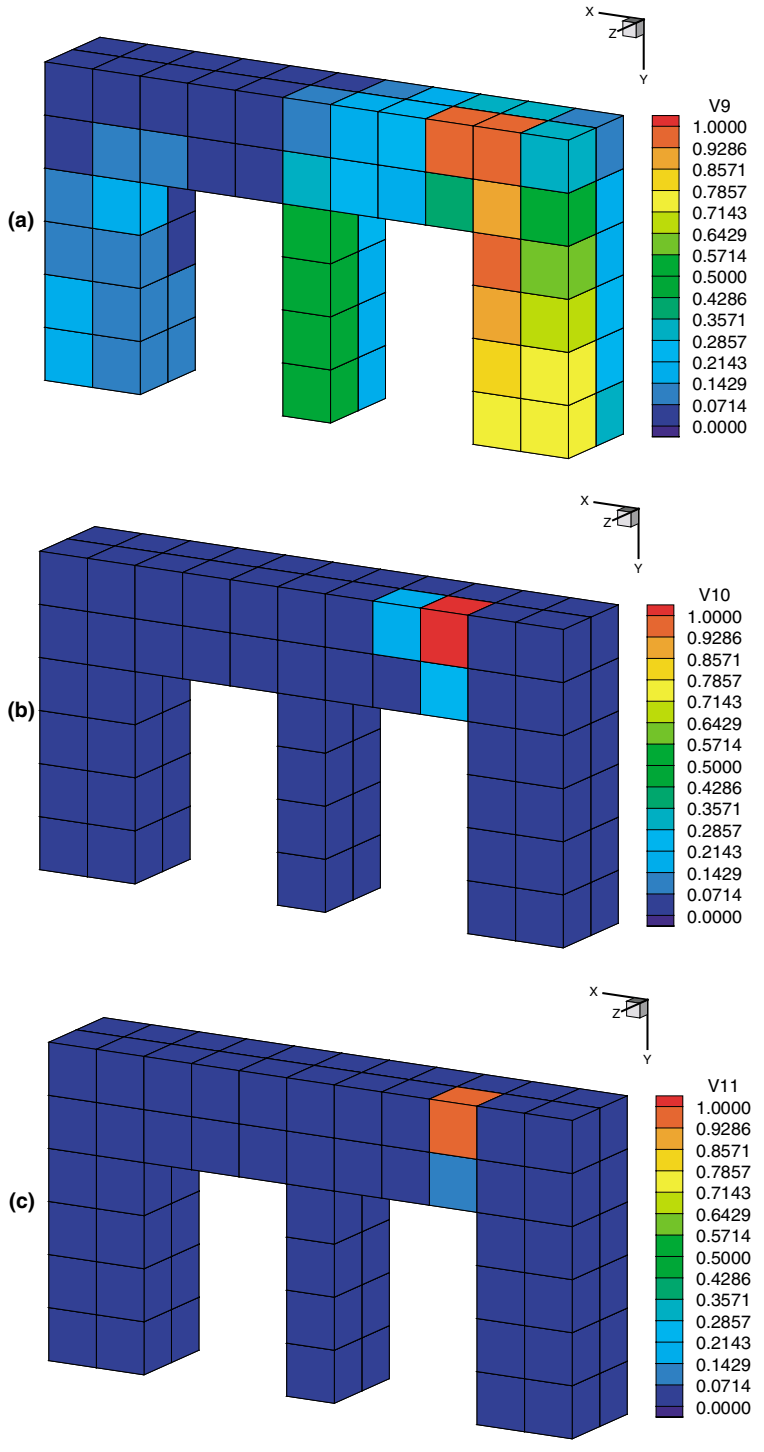

Fig. 13. Example 3: distribution of the normalized error indicators: (a) ζ_k, (b) $\bar{\zeta}_k$, and (c) β_k.

the inclusions is taken to be 0.3. Also, it is assumed that the inclusions are 10 times as stiff as the matrix material. The dashed lines in Fig. 11 indicate the partitioning of the domain into cells.

The quantity of interest here is the σ_{22} component of the stress tensor averaged over ω – an inclusion centered at $\mathbf{x}_0 = (2.75, 0.75, 1.75)m$. The homogenized elasticity tensor is taken to be the average of the

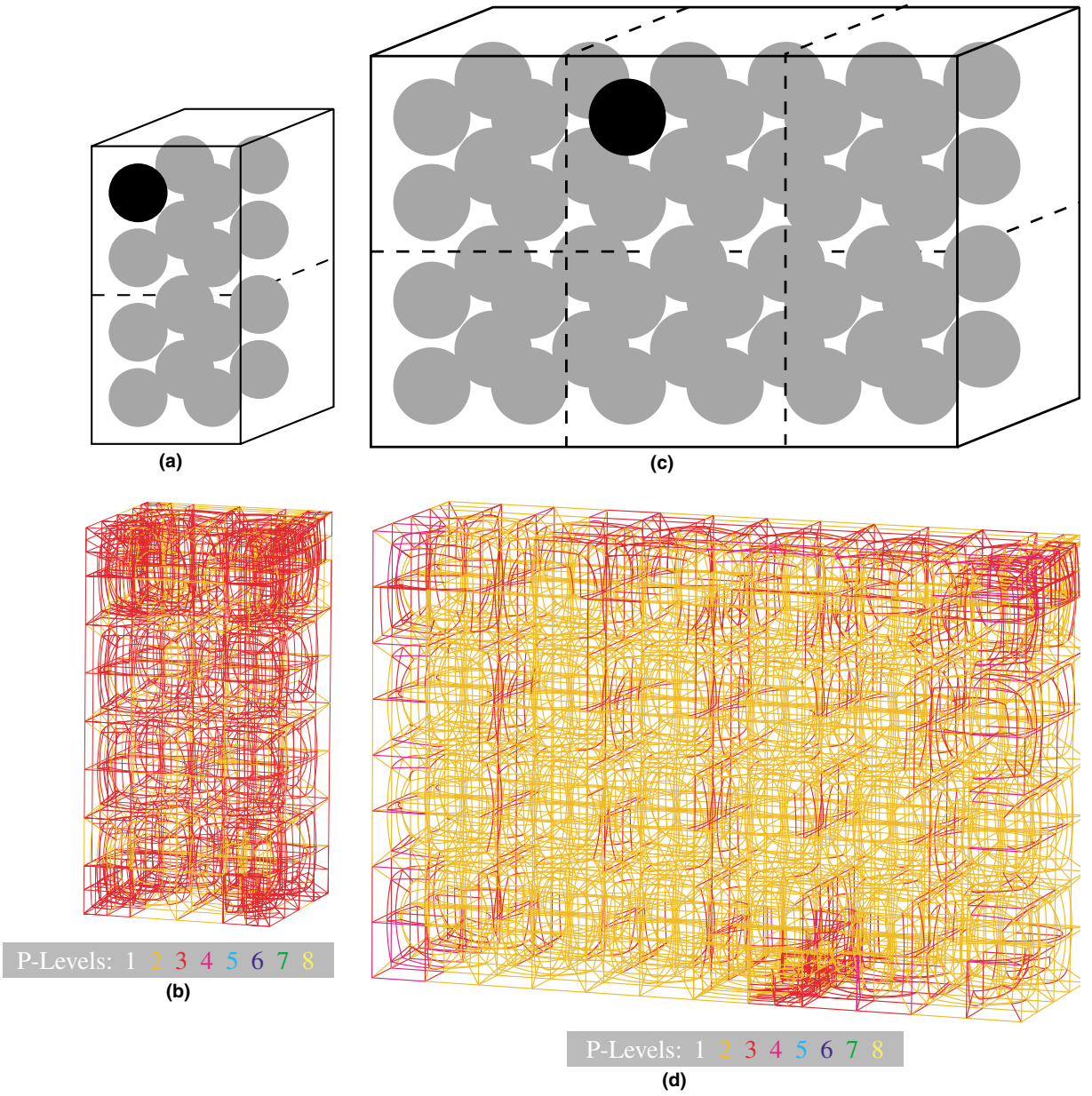

Fig. 14. Example 2: sequence of domains of influence, and hp meshes for the solution of the local fine-scale problem. The inclusion of interest is shown in black.

Hashin–Shtrikman bounds, and the homogenized solutions $\mathbf{u}^0$ and $\mathbf{w}^0$ are computed. The behavior of the normal components of the strain tensor $\boldsymbol{\varepsilon}(\mathbf{w}^0)$ are shown in Fig. 12. In this figure, the values of the functions are shown on three mutually perpendicular planes passing through the center of the inclusion of interest ω.

Next, the modeling error in the quantity of interest is estimated and the modeling error indicators $\zeta_k, \bar{\zeta}_k, \beta_k$ are computed. The estimated relative modeling error in the quantity of interest is 129%. The error indicators ζ_k, $\bar{\zeta}_k$, β_k are shown in Fig. 13. As in the previous example, we see that the error indicators β_k are highly local in nature.

According to the GOALS algorithm, an initial domain of influence is chosen (Fig. 14(a)), and the local fine-scale problem is solved for $\tilde{\mathbf{u}}$. The relative modeling error is now estimated to be 10%. The hp mesh for this domain of influence has 81,000 unknowns, and is shown in Fig. 14(b). The domain of influence is then

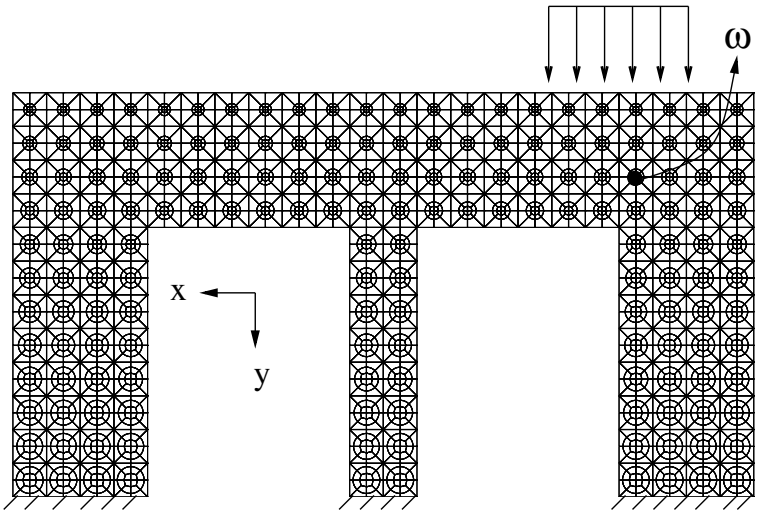

Fig. 15. Example 3: schematic of the problem with nonuniform inclusion volume fraction.

enlarged (Fig. 14(c)), and the local fine-scale problem is re-solved for $\tilde{\mathbf{u}}$, leading to an estimated 4% relative modeling error in the quantity of interest. The hp finite element mesh used for the enlarged domain of influence is shown in Fig. 14(d), and has roughly 130,000 unknowns.

7.3. Example 3

In this example, we test the GOALS algorithm on a problem with a nonuniform volume fraction, provided by a graded distribution of inclusions in a matrix material, as shown by the problem schematic in Fig. 15. The material properties of the constituents are the same as in Example 7.1. The quantity of interest here is the average of the σ_{yy} component of the stress tensor on the inclusion ω indicated in Fig. 15. Thus

$$L(\mathbf{v}) = \frac{1}{|\omega|}\int_{\omega} \sigma_{yy}(\mathbf{v})\,\mathrm{d}\mathbf{x}. \tag{65}$$

The local volume fraction of the inclusions ranges from 0.5 at the bottom of the structure to 0.1 at the top. Of special interest here is the issue of selection of $\mathbf{E}^0$, the homogenized tensor. For the case of periodic materials or for materials that are statistically homogeneous, the selection of $\mathbf{E}^0$ is quite straightforward. However, for the case of nonuniform volume fractions, this is not the case. There are, in general, two criteria for choosing the homogenized elasticity tensor.

1. One possibility is to find the homogenized tensor that minimizes the modeling error in the homogenized solution in a given quantity of interest, assuming that it is possible to find such an $\mathbf{E}^0$ (see [25,31]). This, however, does not guarantee that the resulting modeling error $L(\mathbf{u}-\mathbf{u}^0)$ will be below the tolerance level.
2. The other possibility is to find a homogenized tensor $\mathbf{E}^0$ that provides the best possible boundary conditions to the local problems on the domains of influence Ω_L.

As will be seen, these two criteria are not necessarily compatible. In order to focus on the effect of the homogenized elasticity tensor, we first choose the domain of influence Ω_L, as shown in Fig. 16.

Three different choices of $\mathbf{E}^0$ are considered:

- *Case* A: $\mathbf{E}^0$ is computed based on the volume fraction of inclusions in the immediate neighborhood of the inclusion of interest ω. The inclusion volume fraction here is 0.17.
- *Case* B: $\mathbf{E}^0$ is computed based on the volume fraction in the domain of influence. Here, the inclusion volume fraction is 0.18.
- *Case* C: $\mathbf{E}^0$ is computed based on the volume fraction in the entire domain. The inclusion volume fraction is 0.26.

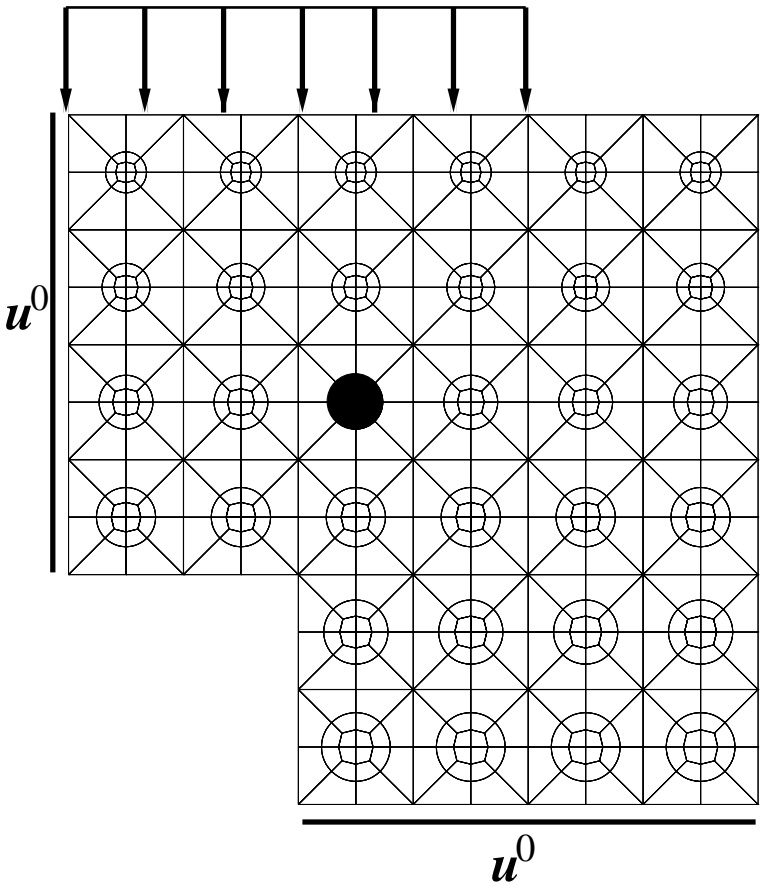

Fig. 16. Example 3: domain of influence Ω_L and the boundary conditions for the local fine-scale problem.

Table 1
Example 3: Effect of $\mathbf{E}^0$ on the quantity of interest

Choice of $\mathbf{E}^0$	$L(\mathbf{u}-\mathbf{u}^0)/L(\mathbf{u})$ (initial error)	$\eta_{\text{est}}/L(\mathbf{e}^0)$ (effectivity index)	$L(\mathbf{u}-\tilde{\mathbf{u}})/L(\mathbf{u})$ (final error)
Case A	1.417	0.78	0.050
Case B	1.321	0.81	0.056
Case C	1.001	0.80	0.096

For each selected volume fraction, we compute the homogenized elasticity tensor $\mathbf{E}^0$ using the lower Hashin–Shtrikman bound. Corresponding to each homogenized tensor $\mathbf{E}^0$, a homogenized solution $\mathbf{u}^0$ is computed and this solution is used as boundary data for the local fine-scale problem for $\tilde{\mathbf{u}}$ on the domain of influence. The results from this process are shown in Table 1. For the purpose of comparison, a reference fine-scale solution is computed on an hp mesh with about 135,000 DOF.

In Table 1, the first column represents the choice of the homogenized elasticity tensor $\mathbf{E}^0$. In the second column, we have the relative modeling error in the quantity of interest in the homogenized solution (modeling error in quantity of interest compared to the true value of the quantity). The third column shows the effectivity index for the local error estimate; the closer it is to unity, the more accurate the error estimate is. In the last column, we have the error in the quantity of interest predicted by the local fine-scale solution $\tilde{\mathbf{u}}$. In case A, we see that the modeling error in the homogenized solution is about 150%, whereas in case C, the modeling error in the homogenized solution is about 100%. In every case, the local estimate of the modeling error is quite accurate. Interestingly, the reduction in the modeling error is more drastic in case A

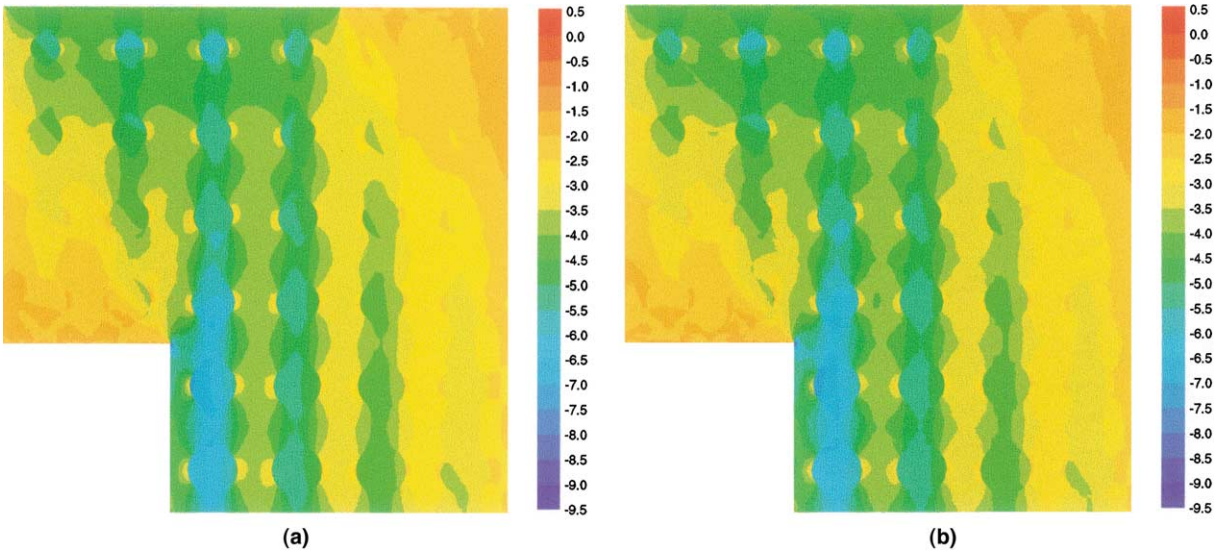

Fig. 17. Example 3: comparison of σ_{yy} stress fields (GPa) predicted by: (a) the local fine-scale solution $\tilde{\mathbf{u}}$, and (b) the reference (global) fine-scale solution $\mathbf{u}$.

than in case C, i.e., even though the quantity of interest predicted by $\mathbf{u}^0$ computed using $\mathbf{E}^0$ of case A is more in error (than case C), it provides better boundary conditions to the local fine-scale problem and thus results in a lower final error in the quantity of interest.

Finally, we compare the σ_{yy} field of the stress tensor predicted by the local fine-scale solution $\tilde{\mathbf{u}}$ and the reference fine-scale solution $\mathbf{u}$ in Fig. 17. The stress field predicted by the local solution $\tilde{\mathbf{u}}$ is essentially similar to the fine-scale stress field except for perturbations near the boundary of the domain of influence. An important conclusion from this comparison is that the local fine-scale solution $\tilde{\mathbf{u}}$ can be used for predicting other local quantities of interest in the neighborhood of the original local quantity.

7.4. Example 4

The problem of adaptively modeling perforated domains, while similar in spirit to the modeling of heterogeneous materials, presents an interesting difference. In all the cases considered so far in this paper and our companion paper [24], the fine-scale and homogenized problems are posed on the same domain Ω. For perforated domains however, this is not the case, since it is domain that gets "smeared out" by the process of homogenization. Thus, the specialized estimates discussed in Section 5.4 must now be employed. Though the error estimates are different, the adaptive modeling procedure and algorithm remain unchanged.

The problem under consideration here is depicted in Fig. 18. As a quantity of interest, we choose the average of the σ_{xx} component of the stress tensor over an annulus A whose inner radius coincides with the void and whose outer radius is 1.2 times the inner radius. The volume fraction of the voids is taken to be 0.3.

$$L(\mathbf{v}) = \frac{1}{|A|}\int_A \sigma_{xx}(\mathbf{v})\,\mathrm{d}\mathbf{x}. \tag{66}$$

The material properties of the perforated domain are taken to be $E = 100$ GPa and $v = 0.2$, and plane strain conditions are assumed. The perforated domain is homogenized using the simple rule of mixtures.

The normal strain fields of the homogenized influence function $\mathbf{w}^0$ are shown in Fig. 19. As in the case of heterogeneous materials (see [24] for a discussion), the behavior of the influence function for perforated domains is also highly local. This roughly means that only local information is required to predict the quantity of interest. This observation is confirmed by the normalized distribution of the local error indicators β_k, shown in Fig. 20.

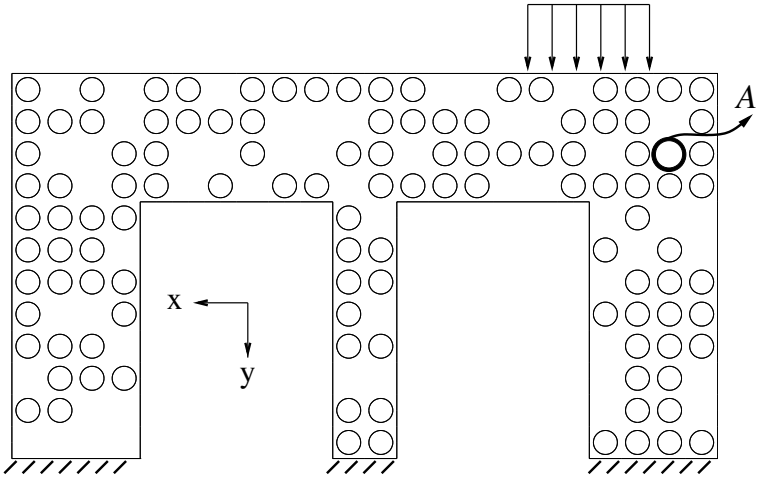

Fig. 18. Example 4: schematic for the perforated domain problem.

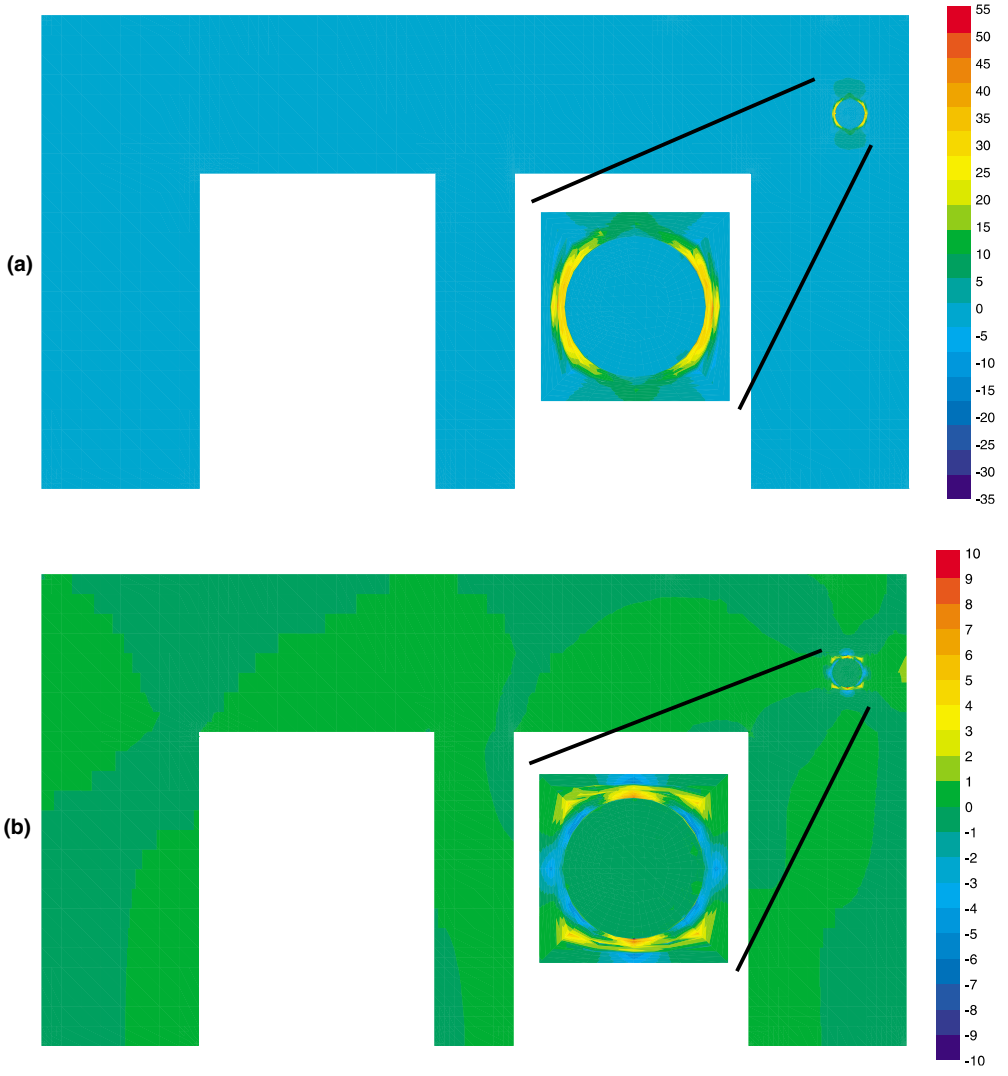

Fig. 19. Example 4: normal strain fields of the homogenized influence function $\mathbf{w}^0$: (a) ε_{xx} and (b) ε_{yy}.

Fig. 20. Example 4: normalized distribution of local error indicator β_k.

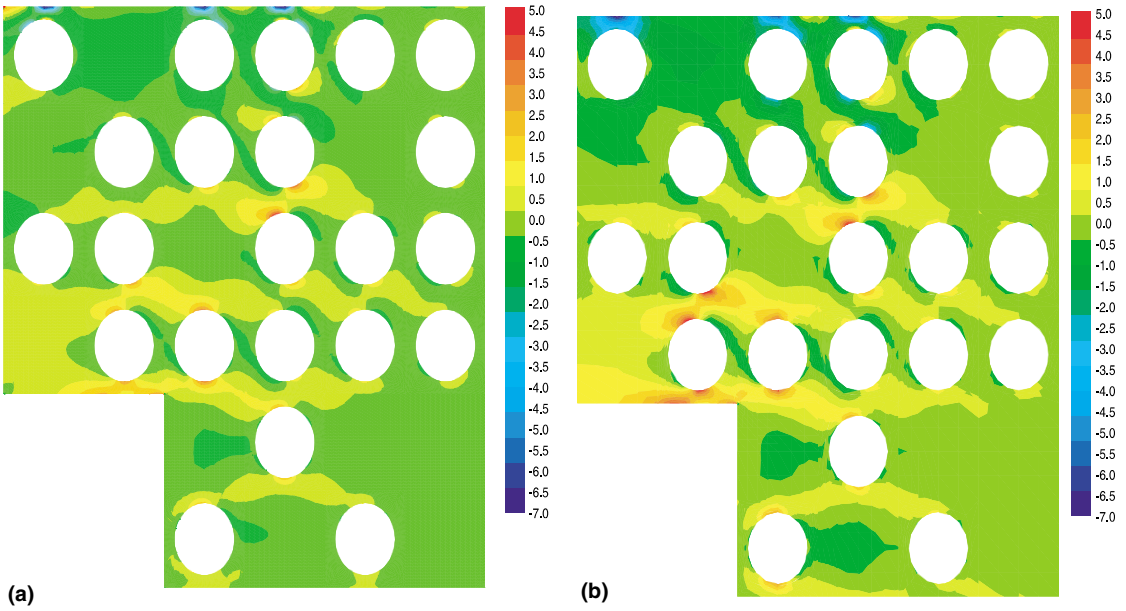

Fig. 21. Example 4: comparison of σ_{xx} stress fields (GPa) predicted by (a) the local fine-scale solution, and (b) the reference (global) fine-scale solution.

The adaptive procedure results in a domain of influence shown in Fig. 21(a). For this size of the domain of influence, the predicted value of the quantity of interest is within 1.2% of the value predicted by the fine-scale solution. Fig. 21 also shows a comparison of the σ_{xx} component of the stress field predicted by the local fine-scale solution $\tilde{\mathbf{u}}$ and the reference fine-scale solution $\mathbf{u}$. Once again, very good agreement is observed, with some perturbations around the boundaries of the domain of influence.

7.5. Example 5

This example demonstrates the integration of two important technologies discussed in this paper: imaging and meshing techniques, and adaptive material modeling. We study the deformation of a fabricated composite material that has a single layer of glass beads ($E = 69$ GPa, $\nu = 0.22$) distributed in an epoxy matrix ($E = 4.6$ GPa, $\nu = 0.36$). The dimensions of the specimen are shown in Fig. 22. The average diameter of the glass beads is 800 μm. Images of the specimen were obtained both with a CT device (resolution $= 10\mu$) and an optical microscope (resolution $= 1\mu$).

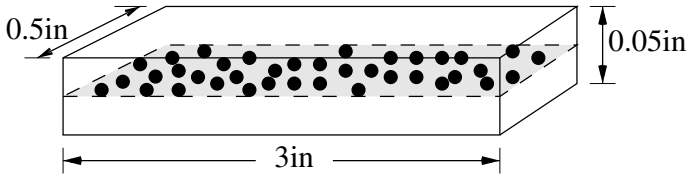

Fig. 22. Example 5: dimensions of the epoxy-glass specimen.

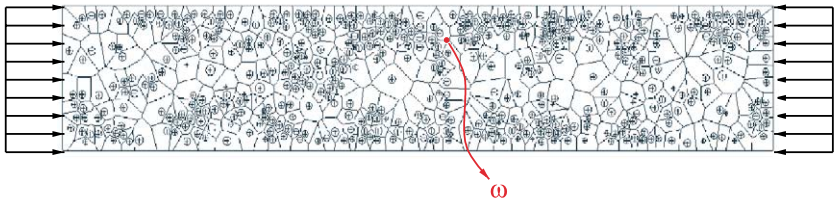

Fig. 23. Example 5: schematic for the 2-D problem of manufactured specimen under compressive loads.

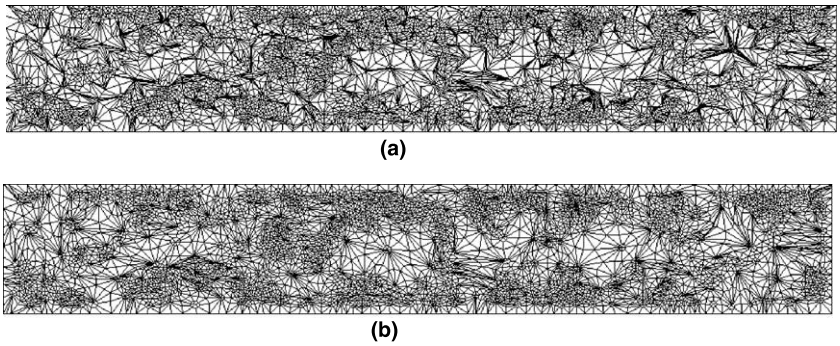

Fig. 24. Example 5: (a) initial mesh, and (b) mesh after smoothing.

We consider the 2-D problem of finding the response of the above specimen to compressive loads, as shown in Fig. 23. We pick, as a quantity of interest, the σ_{xx} component of the stress tensor averaged over the inclusion denoted by ω in Fig. 23.

To compute a reference solution $\mathbf{u}$, the meshing algorithm presented in Section 3 is used to generate a mesh. The resulting initial mesh is shown in Fig. 24(a). The mesh after three iterations of centroid smoothing is shown in Fig. 24(b).

Next, the homogenized primal and adjoint solutions $\mathbf{u}^0$ and $\mathbf{w}^0$ are obtained using the hp finite element code. All three components of the strain tensor of the influence function $\mathbf{w}^0$ are shown in Fig. 25 (recall that the error indicators and estimates involve the strains of the homogenized influence function). As can be seen, the behavior of the strain field is highly local.

The modeling error indicators are then computed and the adaptive procedure is carried out. The sequence of domains of influence and the resulting modeling errors are shown in Fig. 26. Once again, it is seen that the quantity of interest can be predicted accurately using only local microstructural information.

7.6. Example 6

This numerical experiment deals with the analysis of a wrench made of a particulate heterogeneous material, modeled as a 2-D object. An important difference between this example and the previous examples is that the internal microstructure of the body is not known completely. However, as pointed out in

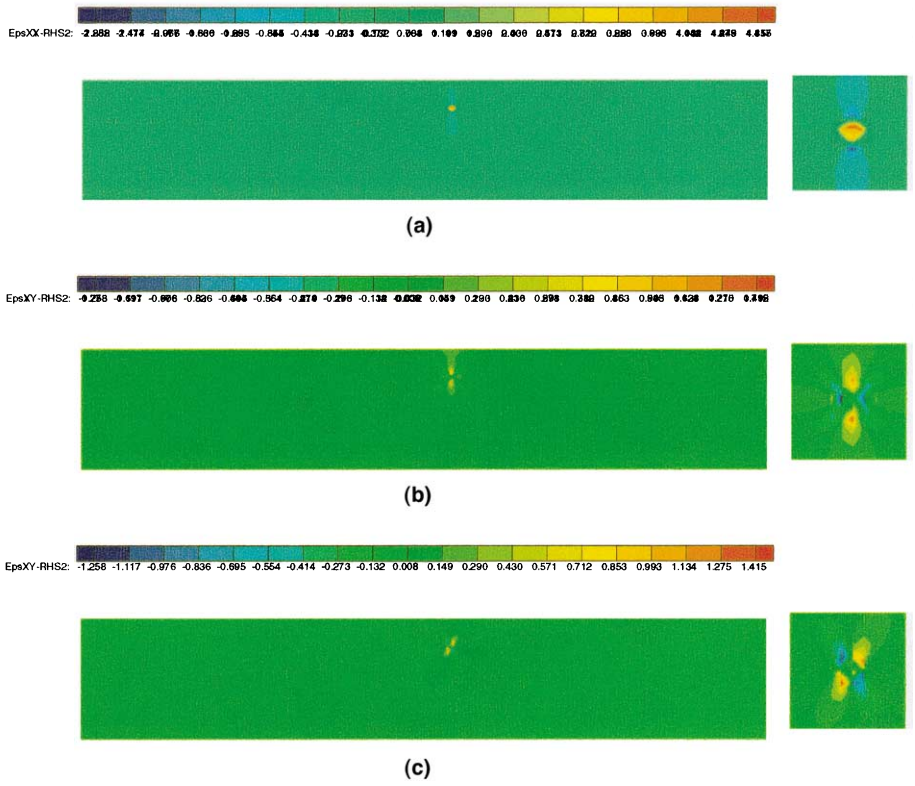

Fig. 25. Example 5: components of the strain tensor of the homogenized influence function $\mathbf{w}^0$: (a) ε_{xx} component, (b) ε_{yy} component, and (c) ε_{xy} component.

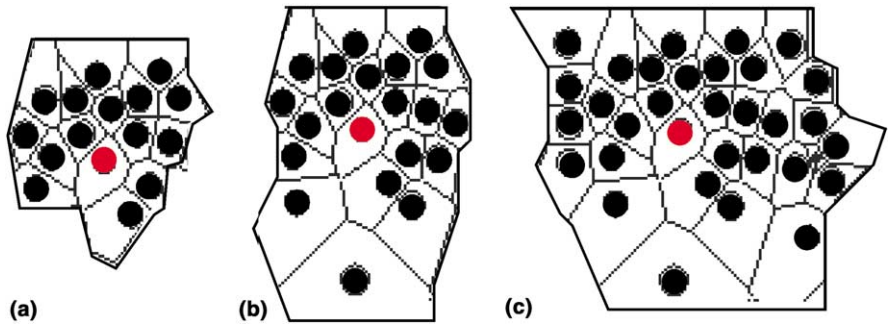

Fig. 26. Example 5: results of the adaptive modeling procedure: domains of influence and resulting modeling errors. (a) % Error = 17.0. (b) % Error = 9.05. (c) % Error = 2.1.

Example 7.1, it is possible to predict local quantities of interest without knowing the microstructure throughout the domain.

Our objective is to study the microscale solution at one corner of the hexagonal part of the boundary of the wrench shown in Fig. 27. A similar problem has been studied by Ghosh and coworkers [8] using the Voronoi Cell finite element method and asymptotic homogenization. The hexagonal part of the boundary is constrained, whereas the circular part of the interior boundary is loaded as shown. The internal microstructure of the wrench is assumed to be known only in the vicinity of the corner of interest, in a circular area of radius 0.04 in. The microstructure in this region consists of randomly distributed circular inclusions, with a local volume fraction of 0.4. Based on the number of inclusions in this region and based on the area of the wrench, it is estimated that the body has about 128,000 inclusions. Judging from results obtained in previous calculations, an adapted hp-FEM mesh of the entire structure sufficient to produce global

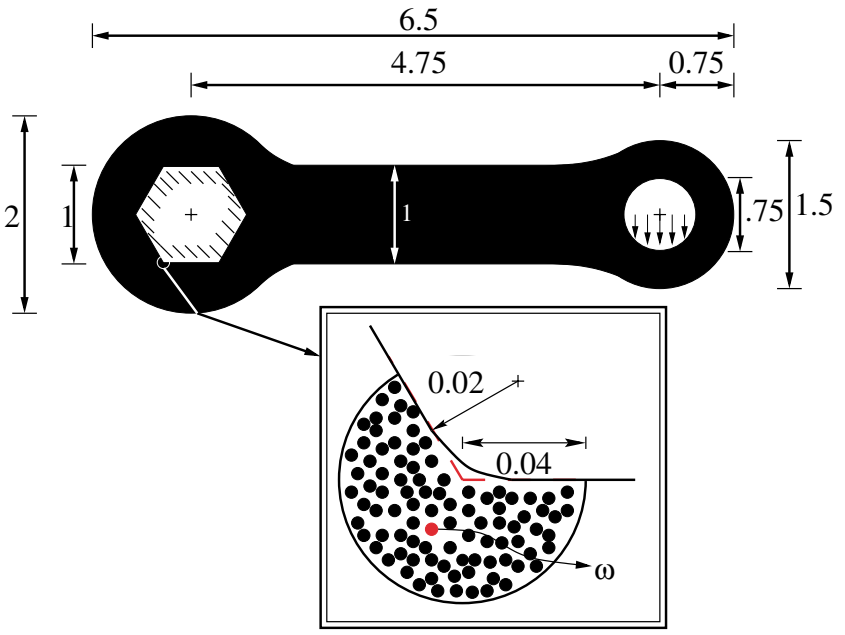

Fig. 27. Example 6: schematic of the wrench. All dimensions are in inches.

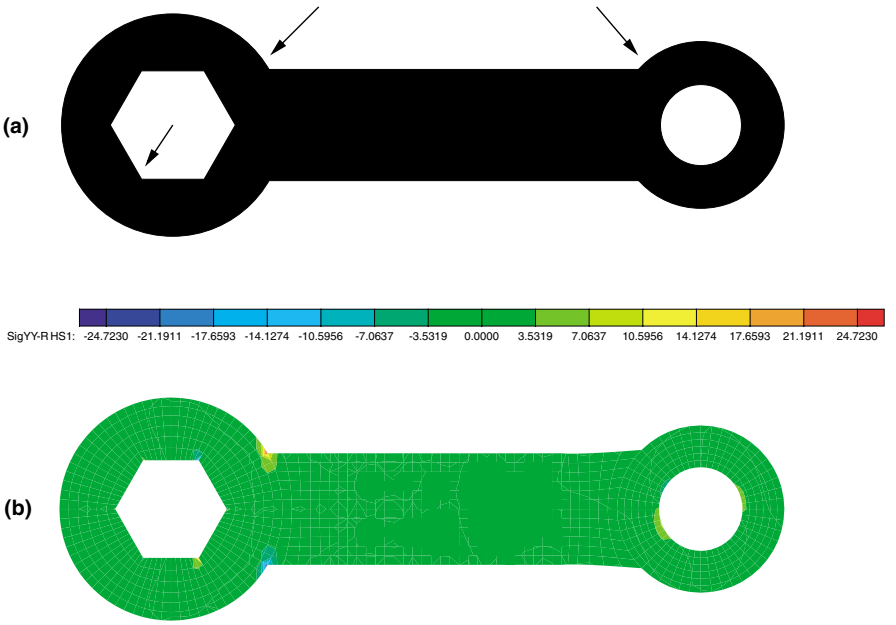

Fig. 28. Example 6: (a) simplified domain for the primal homogenized problem; ignoring fillets (shown by arrows) results in artificial corners, (b) σ_{yy} component of the homogenized stress field (GPa).

solutions within 1% error in an energy norm would require a computational model with on-the-order-of one billion DOF.

The quantity of interest is taken to be the average σ_{yy} stress on the inclusion ω, shown in red. The material properties are taken to be $E = 100$ GPa, $v = 0.2$ for the matrix material, and $E = 1000$ GPa, $v = 0.2$ for the inclusions. The body is homogenized using the Hashin–Shtrikman lower bound. Also, for the homogenized problem, the domain is slightly modified by ignoring the fillets. This simplification is

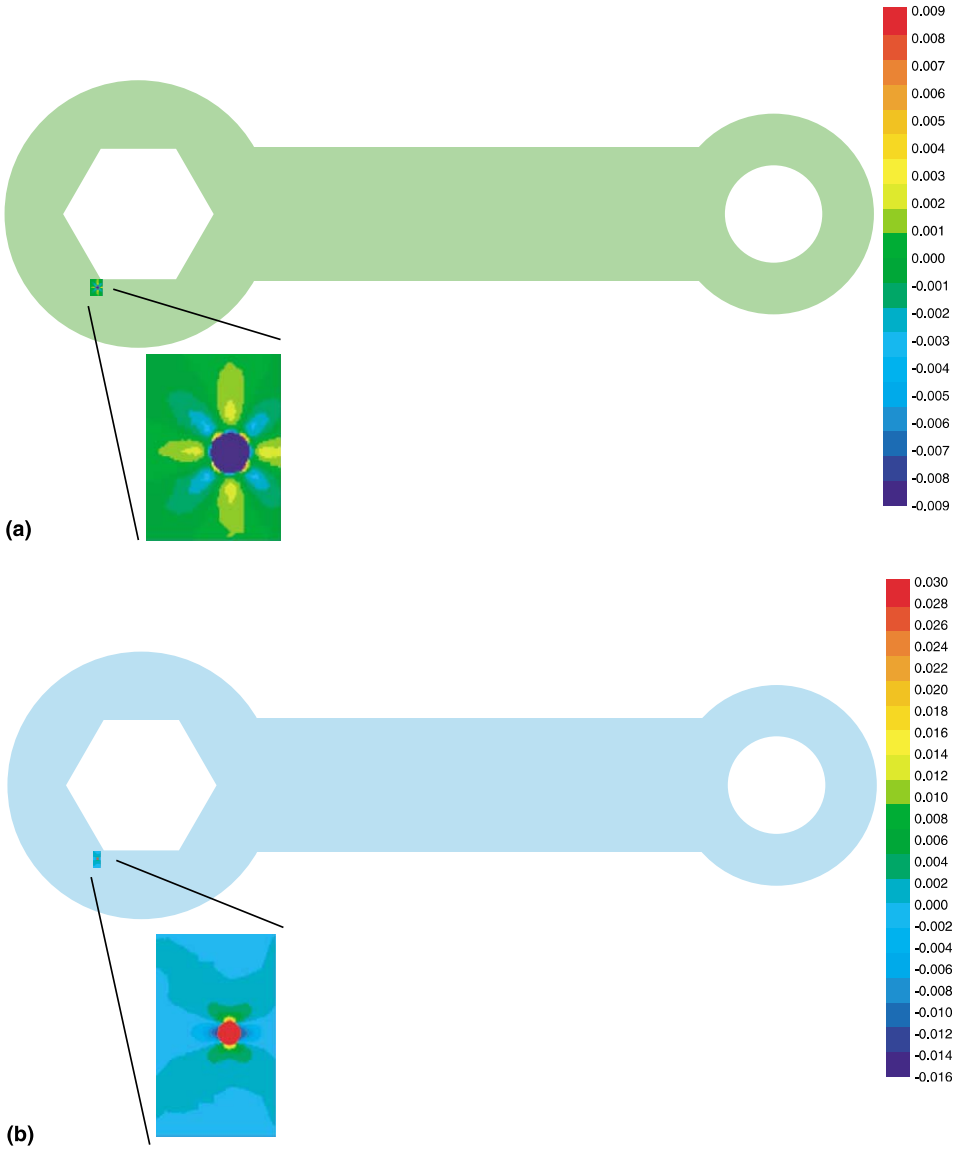

Fig. 29. Example 6: components of strain of the homogenized influence function: (a) ε_{xx} component, and (b) ε_{yy} component.

shown in Fig. 28(a), marked by arrows. This, of course, results in artificial corners in the domain, and hence leads to singularities in the homogenized solution. This is reflected in the plot of σ_{yy} component of the stress tensor, shown in Fig. 28(b).

Next, the homogenized influence function $\mathbf{w}^0$ is computed for the specified quantity of interest. The normal strains of this function are shown in Fig. 29. Once again, a highly local behavior is observed.

Next, the modeling error in the quantity of error is estimated, and $L(\mathbf{e}^0)/L(\mathbf{u}^0)$ is found to be 0.49. The error indicators are then computed and two steps of the adaptive modeling algorithm are carried out. The domains of influence and the resulting estimated modeling errors are shown in Fig. 30. Note that for the local fine-scale problem, the fillet at the vertex of the hexagon is not ignored (Fig. 30(b)).

Thus, knowing only a limited amount of information, the adaptive modeling algorithm allows for the prediction of the quantity of interest to within an estimated 4%.

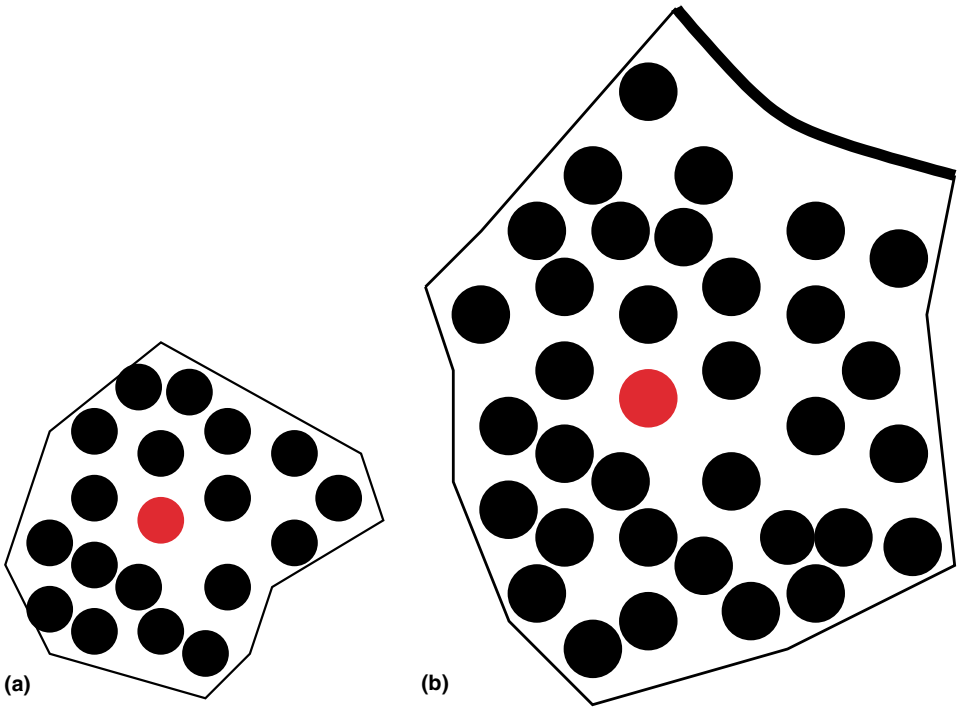

Fig. 30. Example 6: domains of influence and the resulting (estimated) modeling errors in the local solutions: (a) estimated final error = 12.2%; (b) estimated final error = 4.2%.

8. Concluding comments

Much of the work on the mechanics of materials is focused on the analysis of various micromechanical phenomena occurring in small samples of material subject to idealized boundary conditions that are supposed to represent the interaction of the sample with the exterior universe: the complement of some undefined material body. Implicit in such analyses is the assumption that at distances sufficiently far removed from the sample, the material behaves as if it were homogenized, i.e., only averaged properties of material remote from the site of interest affect local behavior in a neighborhood of the site.

There are several major flaws is this traditional procedure. Firstly, exactly how far away from the sample the use of such homogenized properties is valid is unknown. The distance is very much problem dependent, depending on volume fraction and mechanical properties of constituents and numerous other factors, and on how accurately local effects are calculated. Secondly, the approach is usually invalid near boundaries, where external loads, prescribed displacements, and geometrical features of the material body under study can pollute and dominate local behavior.

In the present work, a collection of procedures is presented which makes possible a systematic analysis of heterogeneous bodies. This is accomplished using X-ray images of structural components composed of multi-phase elastic materials to supply data for the GOALS algorithm. This is an adaptive modeling scheme which uses a posteriori estimates of modeling error as a basis for determining the level of microscale information needed in a model in order to deliver local analysis results of a given accuracy. The process makes possible highly accurate analyses of such local micromechanical features such as average stresses on material interfaces.

The effectiveness of the approach is demonstrated on a wide variety of examples in this study. These include example problems with fine periodic microstructure, random nonperiodic two-phase materials, graded materials with nonuniform volume fraction, perforated materials with randomly distributed voids, fabricated composites consisting of a soft epoxy matrix and containing randomly dispersed glass spheres, and an analysis of local average stresses in a composite wrench containing an estimated 128,000 particles.

This latter example demonstrates that the GOALS algorithm can be effective independently of the number of micromechanical constituents.

The extension of the GOALS algorithm to nonlinear problems, such as heterogeneous elasto-plastic materials, is to be the subject of future work.

Acknowledgements

The support of this work by the Office of Naval Research under grant N00014-95-1-0401 and by the Sandia National Laboratories under grant BF-2070 is gratefully acknowledged. The authors also benefited from many discussions and help from Prof. Ivo Babuška, Prof. Chandrajit Bajaj, and Prof. Greg Rodin of TICAM. Much of the work on CT imaging and automatic mesh generation was aided by Prof. Bajaj and his students. Figs. 2 and 3 were kindly provided by Prof. Rodin and Prof. Bajaj, respectively. The hp finite element code which forms a critical component of our GOALS algorithm was built on a framework developed by Prof. Abani Patra of the State University of New York at Buffalo, and his team. We gratefully acknowledge the generous help and advice of Prof. Patra on this aspect of our work. We also express thanks to Dr. Tarek Zohdi for many helpful suggestions. Some computational resources used during the course of this work were provided by the NSF through NPACI, the National Partnership for Advanced Computational Infrastructure.

References

[1] C. Ashcraft, D. Pierce, D.K. Wah, J. Wu, The Reference Manual for SPOOLES, Release 2.2: An Object Oriented Software Library for Solving Sparse Linear Systems of Equations, Boeing Shared Services Group, 1999. Available at www.netlib.org/linalg/spooles/spooles.2.2.html.

[2] I. Babuška, B. Andersson, P.J. Smith, K. Levin, Damage analysis of fiber composites, Part I: statistical analysis of fiber scale, Technical Report FFA TN 1998-15, Flygtekniska Försöksanstalten, Bromma, Sweden, 1998.

[3] C.L. Bajaj, V. Pascucci, Progressive isocontouring, Technical Report TR 1999-36, Texas Institute for Computational and Applied Mathematics, Austin, TX, 1999.

[4] C.L. Bajaj, V. Pascucci, D. Schikore, The contour spectrum, in: Proceedings of the 1997 IEEE Visualization Conference, IEEE, 1997, pp. 167–173.

[5] A. Bensoussan, J.L. Lions, G. Papanicolaou, Asymptotic analysis for periodic structures, Studies in Mathematics and its Applications, vol. 5, North-Holland, Amsterdam, 1978.

[6] R. Christensen, An Introduction to the Mechanics of Composite Materials, Wiley, New York, 1979.

[7] H.C. Edwards, A parallel infrastructure for scalable adaptive finite element methods and its application to least squares *C*-infinity collocation, Ph.D. thesis, The University of Texas at Austin, 1997.

[8] S. Ghosh, K. Lee, S. Moorthy, Two scale analysis of heterogeneous elastic–plastic materials with asymptotic homogenization and voronoi cell finite element model, Comput Methods Appl. Mech. Engrg. 132 (1996) 63–116.

[9] S. Ghosh, S. Moorthy, Particle fracture simulation in non-uniform microstructures of metal–matrix composites, Acta Mater. 46 (1998) 965–982.

[10] W. Gropp, E. Lusk, N. Doss, A. Skjellum, A high-performance, portable implementation of the MPI message passing interface standard, Parallel Comput. 22 (1996) 789–828.

[11] W.D. Gropp, E. Lusk, User's guide for `mpich` a portable implementation of MPI, Mathematics and Computer Science Division, Argonne National Laboratory, 1996, ANL-96/6.

[12] Z. Hashin, Analysis of composite materials, a survey, J. Appl. Mech. 50 (1983) 481–505.

[13] Z. Hashin, S. Shtrikman, On some variational principles in anisotropic and non-homogeneous elasticity, J. Mech. Phys. Solids 10 (1962) 335–342.

[14] Z. Hashin, S. Shtrikman, A variational approach to the theory of the elastic behaviour of polycrystals, J. Mech. Phys. Solids 10 (1962) 343–352.

[15] C. Huet, An integrated micromechanics and statistical continuum thermodynamics approach for studying the fracture behavior of microcracked heterogeneous materials with delayed response, Engrg. Frac. Mech. 58 (1997) 459–556.

[16] V.V. Jikov, S.M. Kozlov, O.A. Oleinik, Homogenization of Differential Operators and Integral Functionals, Springer, Heidelberg, 1994.

[17] A.C. Kak, M. Slaney, Principles of Computerized Tomographic Imaging, IEEE Press, New York, 1988.

[18] B. London, R.N. Yancey, J.A. Smith, High-resolution X-ray computed tomography of composite materials, Mater. Eval. 48 (1990) 604–608.

[19] J.C. Michel, H. Moulinec, P. Suquet, Effective properties of composite materials with periodic microstructure: a computational approach, Comput. Methods Appl. Mech. Engrg. 172 (1999) 109–143.

[20] H. Moulinec, P. Suquet, A numerical method for computing the overall response of nonlinear composites with complex microstructure, Comput. Methods Appl. Mech. Engrg. 157 (1998) 69–94.
[21] J.T. Oden, M. Kuczma, Estimation of modeling error and goal-oriented adaptive modeling for plastic flow problems, Technical Report TR 00-21, Texas Institute for Computational and Applied Mathematics, Austin, TX, 2000.
[22] J.T. Oden, S. Prudhomme, D.C. Hammerand, M. Kuczma, Theory of global estimation of modeling error: first edition, Technical Report TR 00-24, Texas Institute for Computational and Applied Mathematics, Austin, TX, 2000.
[23] J.T. Oden, K. Vemaganti, Adaptive modeling of composite structures: Modeling error estimation, Int. J. Comput. Civil Str. Engrg. 1 (2000) 1–16.
[24] J.T. Oden, K. Vemaganti, Estimation of local modeling error and goal-oriented adaptive modeling of heterogeneous materials; Part I: Error estimates and adaptive algorithms, J. Comput. Phys. 164 (2000) 22–47.
[25] J.T. Oden, T.I. Zohdi, Analysis and adaptive modeling of highly heterogeneous elastic structures, Comput. Methods Appl. Mech. Engrg. 148 (1997) 367–391.
[26] A.K. Patra, J.T. Oden, Problem decomposition strategies for adaptive hp finite element methods, Comput. Syst. Engrg. 6 (1995) 97–109.
[27] W. Rachowicz, J.T. Oden, L.F. Demkowicz, Towards a universal h–p finite element strategy, Part 3. Design of h–p meshes, Comput. Methods Appl. Mech. Engrg. 77 (1989) 181–212.
[28] E. Sanchez-Palencia, Non-homogeneous media and vibration theory, Lecture Notes in Physics, vol. 127 , Springer, Berlin, 1980.
[29] K. Terada, T. Miura, N. Kikuchi, Digital image based modeling applied to the homogenization analysis of composite materials, Comput. Mech. 20 (1997) 331–346.
[30] K. Vemaganti, Modeling error estimation for perforated materials, Technical Report TR 00-25, Texas Institute for Computational and Applied Mathematics, Austin, TX, 2000.
[31] T.I. Zohdi, J.T. Oden, G.J. Rodin, Hierarchical modeling of heterogeneous bodies, Comput. Methods Appl. Mech. Engrg. 138 (1996) 273–298.